Received: 10 February 2022 | Revised: 10 September 2022 | Accepted: 8 October 2022

DOI: 10.1002/we.2789

RESEARCH ARTICLE

WILEY

Large eddy simulations of a utility-scale horizontal axis wind turbine including unsteady aerodynamics and fluid-structure interaction modelling

Giacomo Della Posta[1] | Stefano Leonardi[2] | Matteo Bernardini[1]

[1]Department of Mechanical and Aerospace Engineering, Sapienza University of Rome, Rome, Italy

[2]Department of Mechanical Engineering, University of Texas at Dallas, Richardson, Texas, USA

Correspondence
Giacomo Della Posta, Department of Mechanical and Aerospace Engineering, Sapienza University of Rome, via Eudossiana 18, Rome, RM, 00184, Italy.
Email: giacomo.dellaposta@uniroma1.it

Abstract

Growing horizontal axis wind turbines are increasingly exposed to significant sources of unsteadiness, such as tower shadowing, yawed or waked conditions and environmental effects. Due to increased dimensions, the use of steady tabulated airfoil coefficients to determine the airloads along long blades can be questioned in those numerical fluid models that do not have the sufficient resolution to solve explicitly and dynamically the flow close to the blade. Various models exist to describe unsteady aerodynamics (UA). However, they have been mainly implemented in engineering models, which lack the complete capability of describing the unsteady and multiscale nature of wind energy. To improve the description of the blades' aerodynamic response, a 2D unsteady aerodynamics model is used in this work to estimate the airloads of the actuator line model in our fluid–structure interaction (FSI) solver, based on 3D large eddy simulation. At each section along the actuator lines, a semi-empirical Beddoes-Leishman model includes the effects of noncirculatory terms, unsteady trailing edge separation, and dynamic stall in the dynamic evaluation of the airfoils' aerodynamic coefficients. The aeroelastic response of a utility-scale wind turbine under uniform, laminar and turbulent, sheared inflows is examined with one- and two-way FSI coupling between the blades' structural dynamics and local airloads, with and without the enhanced aerodynamics' description. The results show that the external half of the blade is dominated by aeroelastic effects, whereas the internal one is dominated by significant UA phenomena, which was possible to represent only thanks to the additional model implemented.

KEYWORDS

actuator line model, fluid–structure interaction, large eddy simulation, modal structural dynamics, unsteady aerodynamics

1 | INTRODUCTION

To increase the competitiveness of wind energy, it is fundamental that high-fidelity computational frameworks model progressively all the physical phenomena of real wind turbines.[1] Among the various aspects, wind turbines' aerodynamics is crucial and subjected to many sources of

unsteadiness, such as tower shadowing, yawed conditions, mutual interaction between turbines and fluctuations due to turbulence, topography and atmospheric stability (see Figure 1 for a summary of the various aerodynamic sources). Moreover, the unsteady environment forces the blades' vibration, affecting the aeroelastic response of the wind turbine and in particular of the blades.

It is clear that transient phenomena in the aerodynamics can potentially affect wind turbines, and thus that they should be considered in the numerical modelling. Many studies have highlighted the critical importance of unsteady aerodynamics (UA) phenomena for vertical axis wind turbines (VAWTs).[2,3] However, several works confirmed that one must include UA also for horizontal axis wind turbines (HAWTs) to accurately predict the response of the wind turbine, especially if stall-regulated.[4,5] For example, phenomena like dynamic stall can critically affect the aerodynamic damping limiting the structural vibrations in well-designed rotor blades.[6] Moreover, researchers showed that neglecting UA generates nonexisting flapwise vibrations[7] and that instantaneous aerodynamics in aeroelastic codes can be defective when calculating stalled rotor dynamic performance.[8] Although pitching control reduces the severe load fluctuations due to flow separation, Leishman[9] underlined that load hysteresis with respect to quasi-steady values is observable also if the flow remains attached.

To quantify the *degree of unsteadiness* of the aerodynamic force on an airfoil of semi-chord $b = c/2$, oscillating at an angular frequency ω in a flow with velocity U, the so called *reduced frequency* k is usually introduced:

$$k := \frac{\omega b}{U} = \frac{\omega c}{2U}. \tag{1}$$

According to Leishman,[10] flow unsteadiness can not be neglected if $k > 0.05$, with highly unsteady effects for $k > 0.2$. Vijayakumar et al[11] reported the reduced frequency along the blades of three wind turbines for two typical forcing conditions (Figure 1). It can be seen that for larger wind turbines, flow unsteadiness may become dominant along the entire blade, with severe UA phenomena occurring in the region close to the hub. In fact, by assuming only a slight increase in the tip velocity of the new blades (observed in the latest models) while increasing the rotor diameter, the velocity along a large portion of the span must decrease. Even if the rated rotor speed for larger wind turbines is smaller, this decrease together with the increase in size of the airfoils due to larger blades finally result in an increase of the reduced frequency for forcings easily experienced by the blades. Moreover, induced structural vibrations can cause further unsteadiness, resulting in a nontrivial fluid–structure interaction (FSI), which one should monitor carefully.

Finally, although the Mach number $M = U/a$ is small and the characteristic unsteadiness frequencies are much smaller than the sonic velocity ($Mk << 1$), the possibility of high-k phenomena together with the mild increase in the tip Mach number (below 0.3 in any case), due to rotor upscaling,[12] also signal the potential role of compressibility in UA and for large turbines in general, as highlighted by Yan and Archer.[13]

With computational fluid dynamics (CFD) methods, solving the Navier–Stokes equations allows a proper description of the blades' vorticity shed in the wake. If an appropriate wall-resolved approach with body-fitted grids was then used to solve the flow close to the blades,[14,15] the local and transient response of the boundary layer and its separation would also be described properly. However, the large computational cost required by high-fidelity CFD methods like large eddy simulation (LES),[16] makes this approach currently impractical or at most feasible for one single small turbine.[17] To simulate the large range of scales in the wind energy problem, generalised actuator disc models (GADMs) are commonly used.[18,19] These methods remove the actual solid boundaries of the blades from the fluid domain—and the computational burden related to the necessary fine wall-resolution—and mimic their presence through additional body forces in the Navier–Stokes equations. The body forces are determined by a 2D blade-element approach usually employing steady tabulated data of the airfoil coefficients from wind tunnel measurements. However, this widely adopted approach prevents a complete representation of the transient aerodynamic response of the blade section, which should depend in principle on the complete history of the local Angle of Attack (AoA) and on the complex response of the blade boundary layer. As a result, although GADMs allow an efficient representation of the blades, the insufficient resolution around the airfoil and its simplified

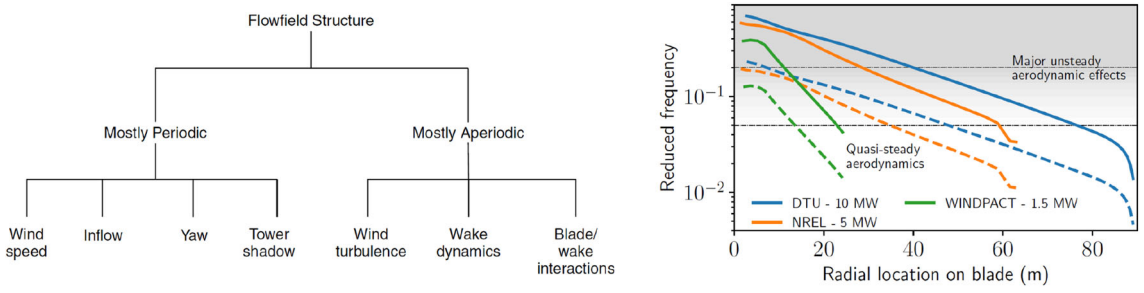

FIGURE 1 Possible aerodynamic sources of unsteadiness for wind turbines' blades (left).[9] Reduced frequencies along the blades of three wind turbines of increasing dimensions and capacities (right).[11] The reduced frequency is defined on the basis of the revolution frequency (dashed) and of three times the revolution frequency (solid)

representation prevent a complete estimation of the aerodynamic loads or airloads. For example, because of dynamic stall phenomena or non-circulatory contributions (see below), the lift coefficient can overcome temporarily its expected value at static stall, depending on the history of the incoming velocity magnitude and direction. However, even by modifying in some way the induced AoA, tabulated airfoil data would never be able to predict the real value, since they are constrained by definition on the steady lift coefficient polar.

The UA phenomena on a 2D airfoil can be classified depending on whether the flow is attached, mildly separated or largely separated. Additional three-dimensional effects due to finite span, rotation and local sweep can alter the airloads too. However, although blades' upscaling could make them more relevant, these three effects have been demonstrated not to be crucial on current wind turbines,[20–23] and so are typically neglected in the majority of the UA models.

Seminal papers[24–29] provided the basis for UA models of 2D airfoils under fully attached flow conditions, mostly in the frequency domain, and showed that high-frequency fluctuations of the AoA can produce significant differences in the airloads relative to their corresponding quasi-steady values. However, time domain formulations are more useful for a generic forcing. According to the *indicial response method*, the loading response to a generic history of the AoA is expressed as the superposition of fundamental indicial aerodynamic responses. With the indicial response ϕ on a thin airfoil undergoing a step change in the AoA α (the Wagner function[25]), the *circulatory* part of the lift, which keeps memory of the complete history of the shed wake, is estimated by a *Duhamel convolution integral* that defines an instantaneous effective AoA. In addition, an *apparent mass* or *noncirculatory* part must also consider the pressure forces required to accelerate the fluid close to the airfoil. This term is derived with different indicial functions[30] and can lead to strong impulsive contributions related to the time derivatives of AoA and pitching rate.[31]

As the AoA increases, however, flow separates unavoidably from the leading or from the trailing edge.

For the latter case, the degree of separation is usually quantified by the nondimensional distance f, such that cf indicates where the separation starts (Figure 2). Usually, f is a function of the AoA, approximated analytically or inferred from steady airfoil data. To model the trailing edge separation, the Kirchhoff 2D plate theory[32,33] is typically adopted. According to this model, the normal and chordwise force coefficients, C_n and C_c, respectively (Figure 2), are expressed as a function of the separation point f and of the attached coefficients for a given AoA. However, if UA is considered, also the degree of separation needs some time to reach its steady value, and hence, the dynamics of f must be considered to include the transient boundary layer response.

Under certain conditions, separation can also start from the leading edge. This phenomenon, the *dynamic stall*, can influence dramatically the lifting properties of the airfoil, and although its complete understanding is still missing,[34] it is widely accepted that it occurs when the effective α varies above and around the static stall angle. The main feature is the development of a leading-edge vortex (LEV):[10] at high angles of attack, the high adverse pressure gradient at the leading edge induces the formation of a vortex that travels progressively along the suction side, prolonging the attached region, until it leaves the trailing edge. The additional lift can produce even 100% overshoots in the maximum lift with an abrupt stall and a large hysteresis in flow reattachment.

The modelling of UA phenomena is still challenging, and researchers agree that at present, a universal UA model does not exist. Even if data-driven methods are promising,[31] the most commonly used approach still consists in using *semi-empirical models* based mainly on the thin-airfoil theory and involving several—more or less—physical–empirical coefficients. Despite being mainly developed for helicopters, several studies proved the ability of these models to describe also wind energy airfoils. The most famous ones are as follows: the ONERA model,[35] the Risø/Hansen model,[36] the Larsen model[37] and the Beddoes–Leishman model.[38] Among them, the latter is undoubtedly the most complete and widespread.

Despite their potential role especially for increasingly long blades, UA models are usually used only in blade element momentum (BEM) solvers and are typically neglected in those state-of-the-art CFD solvers for HAWTs that cannot afford the necessary resolution to solve explicitly

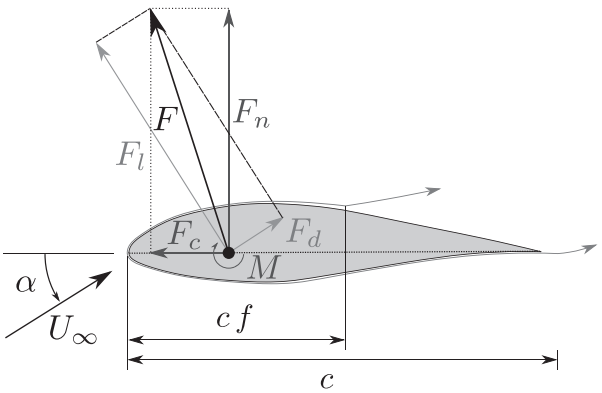

FIGURE 2 Different components of the aerodynamic force F for a generic airfoil. F_n and F_c are the normal and tangent components, while F_l and F_d are the lift and drag components. M is the pitching moment. The nondimensional distance f locates the separation point along the chord

the blades' boundary layer, for example, CFD-GADM solvers, leading to an incomplete description of the local aerodynamic response. In fact, only few studies can be found in the literature trying to implement UA models in GADMs, like the actuator line model (ALM), and they mainly deal with VAWTs,[2,39] with only a very recent work of Spyropoulos et al[40] in the field of HAWTs. However, despite the wide use of validated and calibrated models, the BEM theory relies always on a description of the fluid dynamics that is simplified in comparison with the filtered Navier–Stokes equations solved by the LES approach. At most, potential methods[41] have been similarly used to generate the velocity and AoA in correspondence of the blades, but we think that it is undeniable that if one wants to better characterise the unsteadiness and nonlinearities of the flow field around a wind turbine, exploiting CFD to go beyond the momentum theory usually at the basis of BEM is appealing.

Hence, in this work, we present the implementation of a Beddoes and Leishman (BL) model in our CFD-based FSI solver[42] to complete the description of the 2D aerodynamic response of the blade and to assess its distinct effect on a reference utility-scale wind turbine. Our FSI solver is one of the few in the wind energy literature that is able to join the capabilities of a modal computational structural dynamics (CSD) model with those of an LES fluid model (CFD-CSD method), by exploiting the formulation of a GADM. To characterise the UA effects, we carried out different sets of simulations, with uniform laminar and turbulent sheared inflows and with both rigid and flexible blades.

The paper is organised as follows: Section 2 presents the numerical methodology, including the UA model; Section 3 describes the setup of our simulations, while Section 4 discusses the results; finally, Section 5 highlights the main outcomes of the work.

2 | METHODOLOGY

We present here the methodology used for the simulations. First, we describe our FSI solver and then the added UA model.

2.1 | FSI solver

Our in-house CFD-CSD methodology is based on a two-way coupling procedure between an LES fluid solver and a modal beam-like structural solver, exploiting the representation of the blades in the fluid domain provided by the ALM. As a result, we are able to describe the resulting fluid field with the accuracy of a feasible high-fidelity CFD method, and at the same time, to represent the instantaneous aeroelastic response of the blades by means of an efficient modal CSD method. For further details, see Della Posta et al,[42] where a validation study is also available.

2.1.1 | Fluid model

The flow solver is based on a LES approach for the incompressible Navier–Stokes equations.[43] By adopting the Einstein notation to indicate the components along the x_i axes of the fixed frame of reference (FOR) $\mathcal{R}_e$ (Figure 3), the filtered governing equations are as follows:

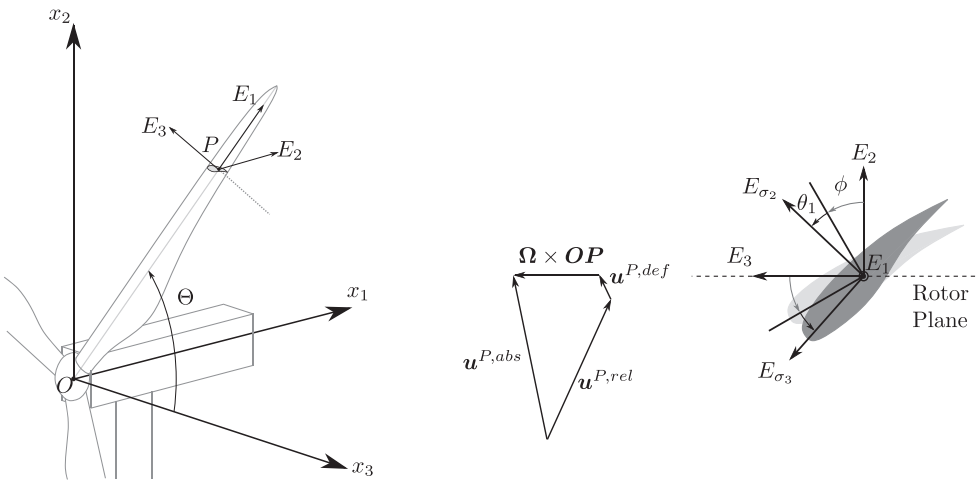

FIGURE 3 Different frames of reference used in the model.[42] The frame $\mathcal{R}_E$ rotates rigidly around the hub centre O of the blades' azimuthal angle Θ (positive counterclockwise). E_2 is constantly directed as the positive streamwise direction. At the generic section P, the pretwist ϕ and the instantaneous angular deformation $\boldsymbol{\theta}$ (only torsion is shown for simplicity) define the local frame of reference $\mathcal{R}_\Sigma$ in which the effective Angle of Attack (AoA) is defined. The different components of the generic velocity vector are shown

$$\frac{\partial \tilde{u}_i}{\partial x_i} = 0, \tag{2}$$

$$\frac{\partial \tilde{u}_i}{\partial t} + \frac{\partial \tilde{u}_i \tilde{u}_j}{\partial x_j} = -\frac{\partial \overline{p}}{\partial x_i} + \frac{1}{Re}\frac{\partial \tilde{u}_i}{\partial x_j \partial x_i} - \frac{\partial \tau_{ij}^d}{\partial x_j} + f_i^t, \tag{3}$$

where we indicate with $\tilde{u}_i$ the filtered velocity components; with $\overline{p}$ the modified pressure, sum of the filtered pressure $\tilde{p}$ and of the isotropic part of the Subgrid-Scale (SGS) tensor $\tau_{ij} = \widetilde{u_i u_j} - \tilde{u}_i \tilde{u}_j = \tau_{ij}^d + \frac{1}{3}\tau_{kk}\delta_{ij}$, which is modelled by the Smagorinsky model[44]; with Re the Reynolds number based on the rotor diameter D, the undisturbed inflow velocity U and the kinematic viscosity of the air ν; with f_i^t the components of the body forces of the turbine modelling. The rotor inside the fluid domain is modelled by the Actuator LineModel (ALM),[45] whereas an Immersed Boundary Method (IBM) procedure, validated in Santoni et al,[46] is used for the tower and the nacelle (see Appendix A1). In compliance with the literature,[47] the spreading parameter ϵ is twice $\Delta(\Delta = \sqrt{\Delta x_1^2 + \Delta x_2^2 + \Delta x_3^2}$, $\Delta x_i = 0.84$m in the isotropic mesh region), and approximately 0.85 the average chord of the blade considered ($\bar{c} \approx 3.47$m). Furthermore, as suggested by Martínez-Tossas et al,[48] a time step constraint is imposed to obtain a smooth application of the actuator body force, such that the actuator line does not span more than one grid cell per time step.

Finite differences are used to discretise the governing equations on an orthogonal staggered grid to prevent odd-even decoupling between pressure and velocity. A fractional step method enforces the incompressibility and allows the evaluation of the pressure, while a hybrid third-order low-storage Runge–Kutta (RK) scheme advances the solution in time, treating implicitly the viscous linear terms and explicitly the remaining nonlinear terms. Second-order accurate, central schemes approximate the space derivative. The code is written in Fortran and is parallelised through the message passing interface (MPI) paradigm.

2.1.2 | Structural model

Since the rotor blades are the most flexible and aerodynamically relevant components of the wind turbine,[49] while the tower and the shaft are rather stiff, the structural model assumes that the only flexible elements are the blades, following a simplified approach widely used in the literature.[50,51] In particular, they are modelled as rotating cantilevered beams clamped at the rotor hub, with small deformations with respect to a relative right-handed FOR $\mathcal{R}_E$ (Figure 3), where E_1 is the direction of the pitching axis, coincident with the neutral axis of the blade passing through the quarter of chord,[52] E_2 is the out-of-plane—or flapwise—direction, pointing at the positive streamwise direction and E_3 is the in-plane—or edgewise—direction.

Under the assumption of linearity, the elastic generalised displacement $\boldsymbol{d}$, which includes translational d_i and rotational θ_i degrees of freedom (DOFs), can be decomposed along the neutral axis coordinate X_1 as follows:

$$\boldsymbol{d}(X_1, t) = \sum_{m=1}^{M} q_m(t)\boldsymbol{\psi}^m(X_1), \tag{4}$$

with $\boldsymbol{\psi}^m(X_1)$ being the m-th elastic mode shape from the modal analysis of the structure, q_m being the corresponding modal coordinate and M being the number of modes considered. Given the decomposition of $\boldsymbol{d}$ in the FOR $\mathcal{R}_E$, d_2 and d_3 are the flapwise and edgewise displacement components, respectively.

The effect of the generic motion of the FOR on the relative structural dynamics (*one-way inertial coupling*, since we assumed that the blade deformation does not modify the rotor inertia) is included in modal basis by means of the methodology introduced in Reschke[53] and further developed for the case of wind energy in Della Posta et al.[42] Through this method, which exploits the decomposition of the acceleration in a moving FOR in the virtual work principle, we obtained a system of elastic equations with additional stiffening, damping and loading terms depending on the angular velocity and acceleration of the rotating FOR (which are determined by means of Equation (A4); see Appendix A1), so that

$$\mathbf{M}\ddot{\boldsymbol{q}} + [\mathbf{D} + \mathbf{D}^{Co}(\boldsymbol{\Omega})]\dot{\boldsymbol{q}} + [\mathbf{K} + \mathbf{K}^{c}(\boldsymbol{\Omega}) + \mathbf{K}^{Eu}(\dot{\boldsymbol{\Omega}})]\boldsymbol{q} = \boldsymbol{e} + \boldsymbol{e}^{c}(\boldsymbol{\Omega}) + \boldsymbol{e}^{Eu}(\dot{\boldsymbol{\Omega}}), \tag{5}$$

where $\mathbf{M}$, $\mathbf{D}$ and $\mathbf{K}$ are the modal structural mass, damping and stiffness matrices, respectively, and $\boldsymbol{e}$ are the external loads in modal basis, including gravity and aerodynamics. The remaining terms are inherently related to the various contributions to the acceleration in a moving FOR: terms with the superscript *Co*, *c* and *Eu* are related, respectively, to the Coriolis, centrifugal and Euler accelerations. The discrete evaluation of the additional inertial terms in Equation (5) is expressed as a function only of the information known from the structure finite-element method (FEM) model and from the corresponding mode shapes, according to Saltari et al.[54] With the present modal approach, if one considers modal displacement, deformation velocity and acceleration and given the modal shapes of the structure, the total number of variables handled at runtime for the structural dynamics of each blade is equal to $3 \cdot M$, which is usually a very small number.

For the modal analysis, the finite element model of the blade used was based on complete beam elements with 6 DOFs, with Euler–Bernoulli behaviour for edgewise and flapwise bending and linear shape functions for axial and torsional deformations.[55] The second-order accurate generalised-α method[56] advances the solution in time.

2.1.3 | FSI model

The two-way coupling aeroelastic model exploits the ALM sectional approach by locally modifying the AoA and the relative velocity according to the instantaneous blade motion given by the structural dynamics. The interested reader can refer to Della Posta et al[42] for further information about the coupling procedure. Here in the following, we report only a short summary of the method.

The method uses a loose partitioned coupling,[57] which proved to be sufficient for wind energy,[58] and joins the two independent or *partitioned* solvers running in parallel through a parallel staggered algorithm.[59] In particular, the distribution of the AoA along each blade is evaluated not only as a function of the velocity field from the fluid solver and of the angular velocity from the rotor dynamics but also as a function of the instantaneous elastic state (see Equation (7)). The latter is in general made of the deformation velocity $\boldsymbol{v} = \dot{\boldsymbol{d}}$ and of the local vector of the deformation angles $\boldsymbol{\theta}$ (torsion and bendings) coming from the structural solver, which is forced by the updated aerodynamic forces.

The algorithm limits the interfield communications only at the beginning of each RK substep and so is highly efficient from a computational point of view. Although the method is not exactly conservative, as almost all partitioned methods,[60,61] Farhat and Lesoinne[59,62] showed that by using a sufficiently small time step, the partitioned algorithm adopted introduces negligible errors compared with more complex coupling algorithms that have superior accuracy and conservation properties[57] but that require consecutive re-evaluations of the structural and fluid solvers to improve the estimation of the aerodynamic forces and of the elastic state. In fact, the stringent time step limitation required by ALM, mentioned in Section 2.1.1, imposes a time step that is much smaller than the one required by the dominant structural unsteadiness of the blades and proved also to be sufficient for the complete FSI algorithm to avoid any kind of numerical instability in all our simulations. As a result, the knowledge of the aerodynamic loading at the fine temporal resolution of the fluid scheme was used to increase the accuracy and stability of the structural scheme and in general of the FSI algorithm, preserving the overall efficiency of the code.

Although the FSI implementation allows more general coupling approaches, following at first the assumption already used in other works,[63,64] in this study, we consider a two-way coupling that includes the effect of the blade deformation velocity only. We decided to neglect also the effect of the torsional dynamics on the basis of our previous results on the effect of torsion,[42] which revealed the reduced dynamical effect of this DOF for blades that are torsionally stiff like the ones considered in this work and given the questionable results obtained in terms of pitching moment from the UA model (see Section 4.2). In general, the relative velocity for a moving blade can be written as follows:

$$\boldsymbol{U_{rel}} = \boldsymbol{u} - \boldsymbol{\Omega} \times \boldsymbol{R_{OP}} - \boldsymbol{v}, \tag{6}$$

where $\boldsymbol{u}$ is the filtered velocity from the fluid solver at the actuator line, $\boldsymbol{R_{OP}}$ is the position vector pointing to the section considered and $\boldsymbol{v}$ is the deformation velocity of the structure at that position. As a result, the relative velocity magnitude and the AoA used to determine the airload coefficients (Equations (A1)) are as follows:

$$\alpha = \operatorname{atan}\left(\frac{\boldsymbol{U_{rel}} \cdot \boldsymbol{E}_2}{-\boldsymbol{U_{rel}} \cdot \boldsymbol{E}_3}\right) - \phi = \operatorname{atan}\left[\frac{(\boldsymbol{u} - \boldsymbol{v}) \cdot \boldsymbol{E}_2}{\Omega r - (\boldsymbol{u} - \boldsymbol{v}) \cdot \boldsymbol{E}_3}\right] - \phi, \text{and} U_{rel} = \sqrt{(\boldsymbol{U_{rel}} \cdot \boldsymbol{E}_2)^2 + (\boldsymbol{U_{rel}} \cdot \boldsymbol{E}_3)^2}, \tag{7}$$

where $\boldsymbol{E}_i$ are the versors of the relative FOR rotating with the structure $\mathcal{R}_E$, and hence, $v_2 = \boldsymbol{v} \cdot \boldsymbol{E}_2$ is the flapwise deformation velocity component, and $v_3 = \boldsymbol{v} \cdot \boldsymbol{E}_3$ is the edgewise deformation velocity component.

Similar to other works,[64,65] the simplified coupling procedure profits from the sectional 1D formulation of the ALM and avoids the complex fluid–solid interface treatment with the associated kinematic and traction conditions.[66] Moreover, the efficient coupling algorithm and structural solver are able to preserve the overall computational efficiency, already loaded with the considerable expense of the LES.

2.2 | UA model

Given its completeness and extensive use in the literature, also for the wind turbine under study,[67] we decided to implement the semi-empirical model of Beddoes and Leishman[38] to complete the description of the aerodynamic sectional forces in the ALM blade-element approach. Despite the obvious limitations in the accuracy of a semi-empirical model[36,37,68] and the use of constants that should be tuned to experimental data, the model has a limited complexity but maintain a physical meaning and has proved to provide reliable results.[23]

The specific implementation chosen for this work is based on the paper of Damiani and Hayman,[67] to which we refer the reader for additional information. The model relates the normal force, the chordwise force, and the pitching moment coefficients, C_n, C_c, and C_m respectively, to the history of the AoA α, and its time derivatives $\dot{\alpha}$ and $\ddot{\alpha}$, normalised and approximated at time n by the backward finite difference expressions $K_{\alpha n} = (\alpha_n - \alpha_{n-1})/\Delta t$ and $K_{q_n} = (q_n - q_{n-1})/\Delta t$, where $q = \dot{\alpha}c/U$ is the pitch rate. The original method includes compressibility, and it is made of three submodules modelling the unsteady attached flow response (*pot* contributions), the unsteady trailing edge separation (*fs* contributions) and the dynamic stall (*v* contributions). The three aerodynamic coefficients are thus given by the following:

$$C_n = C_n^{fs} + C_n^{v} = C_n^{fs,c} + C_n^{pot,nc} + C_n^{v} \tag{8a}$$

$$C_c = C_c^{fs} + C_c^{v} = C_c^{fs,c} + C_c^{pot,nc} + C_n^{v} \tag{8b}$$

$$C_m = C_m^{fs} + C_m^{v} = C_m^{fs,c} + C_m^{pot,nc} + C_m^{v}. \tag{8c}$$

The superscripts *c* and *nc* indicate the circulatory and noncirculatory components of the airloads. The total generic airload coefficient from the module of the base attached flow response, $C_\bullet^{pot}$, is given by the sum of the circulatory $C_\bullet^{pot,c}$ and noncirculatory $C_\bullet^{pot,nc}$ parts.

2.2.1 | Unsteady attached flow

According to the original model, the unsteady response of the attached flow is given by the superposition of indicial responses to step variations in the forcing, defined by exponential circulatory and noncirculatory functions. However, since our method couples the UA module to an LES solver, the shedding of the vorticity in the wake is already explicitly solved, and so the circulatory effects are already included in the local kinematics of the flow used to determine the instantaneous AoA. Moreover, the noncirculatory terms of the original—compressible—model tend to infinite when the Mach number goes to zero. For this reason, to avoid too large concentrated forces especially close to the hub where velocities are small, we used the incompressible Theodorsen theory[69] to express the noncirculatory terms. The absence of compressibility effects makes the added mass terms related only to the instantaneous value of the time derivatives of AoA.

According to the above assumptions, the circulatory part of the normal force is simply given by the following:

$$C_n^{pot,c} = \frac{C_{n\alpha}}{\beta_M}(\alpha - \alpha_0), \tag{9}$$

where $C_{n\alpha}^{c}$ is the slope of the linear portion of the $C_n - \alpha$ curve, $\beta_M = \sqrt{1 - M^2}$ is the Prandtl–Glauert factor, α is the AoA from Equation (7) and α_0 is the zero-lift AoA. The added mass terms in the normal force coefficient for arbitrary free-stream velocity fluctuations[70] are instead:

$$C_n^{pot,nc} = \frac{\pi b}{U^2}\left[\ddot{h} + \frac{\mathrm{d}(U\alpha)}{\mathrm{d}t} + \frac{b}{2}\ddot{\alpha}\right], \tag{10}$$

where $b = c/2$ is half the local chord, U is the relative velocity and h is the plunge displacement. The above equations has been discretised adopting a backward finite-difference and assuming that the blade motion is already included in Equation (7).

On the other hand, since the noncirculatory part is not relevant for the drag ($C_c^{pot,nc} = 0$),[10] and the D'Alambert paradox imposes a null drag in potential flows ($C_c = C_n \tan\alpha$), the chordwise force from the attached flow module is as follows:

$$C_c^{pot} = C_n^{pot,c} \tan\alpha. \tag{11}$$

The circulatory part of the total unsteady pitching moment for attached flow at the quarter of chord is instead given by:

$$C_m^{pot,c} = C_{m0} - \frac{C_{n\alpha}}{\beta_M}\phi_\alpha^c(\hat{x}_{ac} - 0.25), \tag{12}$$

where $\hat{x}_{ac}$ is the aerodynamic centre position from the leading edge, C_{m0} is the pitching moment coefficient at zero lift and ϕ_α^c is the Jones' approximation of the circulatory response function.[71] We then express also the noncirculatory contributions of the pitching moment according to the incompressible theory. In general, the added-mass terms of the pitching moment, referred to $c/4$, are as follows:

$$C_m^{nc} = \frac{\pi}{2}\left(-\frac{b\ddot{h}}{2U^2} - \frac{3}{8}\frac{b^2\ddot{\alpha}}{U^2} + \frac{\dot{h}}{U} + \alpha\right). \tag{13}$$

2.2.2 | Unsteady trailing edge separation

The BL model describes then the dynamic flow separation at the trailing edge by means of the Kirchhoff's theory. On the basis of the modifications proposed by Moriarty and Hansen[41] and Liu et al[72] for large $|\alpha|$, the normal and chordwise force coefficients are given by the following:

$$C_n^{fs,c} = C_n^{pot,c}\left[\frac{1+\text{sign}(f_n)\sqrt{\text{abs}(f_n)}}{2}\right]^2, \tag{14a}$$

$$C_c^{fs,c} = \eta_e C_c^{pot,c}\,\text{sign}(f_c)\sqrt{\text{abs}(f_c)}\tan\alpha. \tag{14b}$$

where η_e is a recovery factor to consider viscous effects and $f_n(\alpha)$ and $f_c(\alpha)$ are the two separation point distance functions obtained by inverting Equations (14a) and 14b using the experimental airfoil data. The procedure used to evaluate the actual separation points used in Equations (14) is such to include the effects of the lagged response of the boundary layer dynamics in the circulatory force component.

As a first step, an effective separation point is interpolated on the $\alpha - f_n$ curve in correspondence of an effective AoA α_f incorporating the unsteady pressure response. A first-order lag on C_n^{pot} thus evaluates an effective C_n':

$$C_n' = C_n^{pot} - D_p \text{ with } D_{p_n} = D_{p_{n-1}}\exp(-\Delta s/T_p) + (C_{n,n}^{pot} - C_{n,n-1}^{pot})\exp[-\Delta s/(2T_p)], \tag{15}$$

where D_p is a deficiency function, T_P is an empirical time constant and s is the *reduced time* ($s = \int_0^t U/b\,dt$). The effective AoA α_f is thus:

$$\alpha_f = \frac{C_n'}{C_{n\alpha}^c/\beta_M} + \alpha_0. \tag{16}$$

Given the effective value of the separation point $f' = f_n(\alpha_f)$, the definitive separation point f'' used for Equation (14a) is found by considering the additional delay in the boundary layer response given by the deficiency function D_f and regulated by an another empirical time constant T_f. Analogously, one has the following:

$$f'' = f' - D_f \text{ with } D_{f_n} = D_{f_{n-1}}\exp(-\Delta s/T_f) + (f_n' - f_{n-1}')\exp[-\Delta s/(2T_f)]. \tag{17}$$

Once the separation point f'' is estimated, one should invert the $\alpha - f_n$ curve in correspondence of the f'' value, to evaluate the value of the f_c curve at $\alpha(f'') = f_n^{-1}(f'')$. However, to avoid inverting the noninjective function $f_n(\alpha)$, inspired by Sheng et al,[68] we apply a first-order lag directly to the effective angle α_f:

$$\alpha'' = \alpha_f - D_\alpha \text{ with } D_{\alpha_n} = D_{\alpha_{n-1}}\exp(-\Delta s/T_f) + (\alpha_{fn} - \alpha_{fn-1})\exp[-\Delta s/(2T_f)], \tag{18}$$

where we introduce the deficiency function D_α and we assume that T_f is the same time constant regulating the boundary layer delay in Equation (17) and that $\alpha(f'') \approx \alpha''$. Finally, we interpolate the chordwise-defined separation point location $f_c'' = f_c(\alpha'')$ used in Equation (14b).

The pitching moment coefficient is instead evaluated following Leishman,[73] which keeps Equation (12) unaltered and substitutes only x_{ac} with the position from the leading edge of the centre of pressure $\hat{x}_{cp}$. In order to recover the measured data in the limit steady case, we use a look-up table defined on the basis of the steady tabulated aerodynamic data (indicated with the subscript *st*). Since also the $\hat{x}_{cp}(\alpha)$ function is not injective, the model uses the angle α'' to interpolate the delayed effective centre of pressure position. As a result, the expression of the total pitching moment becomes:

$$C_m^{fs,c} = C_{m0} - \frac{C_{n\alpha}}{\beta_M}\phi_\alpha^c(\hat{x}_{cp} - 0.25). \tag{19}$$

2.2.3 | Dynamic stall

The final module includes the effects induced by the formation of a LEV that originates, convects along the airfoil and then detaches.

Although different conditions have been proposed to establish when the vortex is generated,[68] we decided to maintain the criterion of the original BL model, based on the value of the steady normal force in correspondence of the break of the chordwise force at the onset of stall.

Once determined that the leading-edge separation is occurring, a nondimensional time variable τ_V tracks the position of the vortex along the upper surface of the airfoil with respect to the empirical time constant T_{VL}, which indicates the time needed by the vortex to travel from the leading edge to the trailing edge.[37,74] When $\tau_V > T_{VL}$, the vortex has been shed in the wake, and so vorticity is no longer accumulated. Multiple shedding can take place at a certain shedding frequency, defined by the Mach-independent Strouhal number $St_{sh} \approx 0.19$.

When dynamic stall is taking place and the vortex is on the profile, the normal force component receives an additional contribution: regulated by another first-order time lag:

$$C^v_{n,n} = C^v_{n,n-1} \exp(-\Delta s/T_V) + (C_{V_n} - C_{V_{n-1}}) \exp[-\Delta s/(2T_V)], \tag{20}$$

where $C_V = C^{pot,c}_n - C^{fs,c}_n$ and T_V is the time constant related to the decay of the vortex lift.

When dynamic stall is instead not taking place or when the vortex has left the airfoil, an accelerated decay is imposed on C^v_n:

$$C^v_{n,n} = C^v_{n,n-1} \exp[-\Delta s/(T_V/2)] \tag{21}$$

For what concerns the chordwise force component, we adopt the method presented by Pierce,[75] where

$$C^v_c = C^v_n \tan(\alpha_e)(1 - \tau_V/T_{VL}). \tag{22}$$

For the pitching moment, Leishman[73] represents the additional contribution from the dynamic stall as follows:

$$C^v_m = -\hat{x}^v_{cp} C^v_n, \text{with} \hat{x}^v_{cp} = \bar{\bar{x}}_{cp}[1 - \cos(\pi\tau_V/T_{VL})], \tag{23}$$

where $\hat{x}^v_{cp}$ is the distance of the centre of pressure from the quarter of chord and $\bar{\bar{x}}_{cp}$ is an airfoil-dependent constant usually set at 0.2.

Finally, one last comment regarding the communication of the vortex shedding to the flow. Although the dynamic stall involves the generation and advection in the wake of the LEV, it is important to stress that ALM is in principle able to consider the effects of vortex shedding from the blades only indirectly. In particular, for the specific case of the dynamic stall, the linear increase in the lift, due to the convection of the vortex along the chord, is the only effect perceived and transferred to the fluid by the actuator line's body forces, without the explicit definition of a LEV. Indeed, the localised increase in body force represents a source of vorticity in the fluid equations with the right circulation resulting from the imposition of the tabulated or modelled aerodynamic forces.

3 | SETUP

In this work, we examine the reference NREL 5 MW wind turbine[52] (properties in Table 1).

On the basis of our previous work, the dimensions of the fluid computational domain (Figure 4) are $L_x \times L_y \times L_z = 9.0D \times 10.0D \times 2.88D$, discretised by an orthogonal mesh of $N_x \times N_y \times N_z = 1296 \times 432 \times 432$ points. While the spacing is uniformly distributed in the streamwise and the spanwise directions, and in the first 2*D* in the vertical direction, to obtain an isotropic mesh in the rotor region, the remaining wall-normal spacing is stretched to limit the grid requirements. Simulations with the same domain but with 50, 150 and 200 points per diameter provided similar results, except for a reduced resolution in the first case and an unfeasible computational cost in the latter case. Hence, we opted for the intermediate mesh, which provides a compromise between accuracy and computational cost. The turbine is at the spanwise centre and at $X_t = 3.5D$ from the inlet.

Periodic, free-slip and radiative boundary conditions are imposed on the lateral, top and outlet surfaces respectively, whereas a Van Driest damping function[76] corrects the flow close to the no-slip bottom wall. Finally, we consider two inflows: in the first, we impose a uniform velocity $U = 10\text{m/s}$, while in the second, we impose a sheared turbulent velocity representative of a turbulent atmospheric boundary layer (ABL). On the basis of the review of Breton et al,[77] we derived the inflow turbulent fluctuations from a precursor simulation in a fully periodic channel with cubic surface roughness,[78] and we superimposed an appropriate power law $(U/U_{hub} = (y/y_{hub})^{\alpha})$ with shear exponent $\alpha = 0.20$ and mean hub velocity $U_{hub} = 10\text{m/s}$. The turbulence intensity at hub height is approximately $TI \approx 10\%$. In order to check the quality of the generated inflow with respect to widely used synthetic turbulence models, we also compared the spectral features of the obtained velocity fluctuations with the results of the Mann turbulence model,[79,80] obtaining a satisfactory agreement.

TABLE 1 Gross properties of the NREL 5 MW wind turbine[52]

Parameter	Symbol	Value	Units
Rated power	P^r	5	MW
Rated wind speed	U^r	11.4	m/s
Rated angular speed	Ω^r	1.27	rad/s
Rotor diameter	D	126.0	m
Blade length	L	61.5	m
Hub height	h	90.0	m
Blade mass	m_b	17740	kg

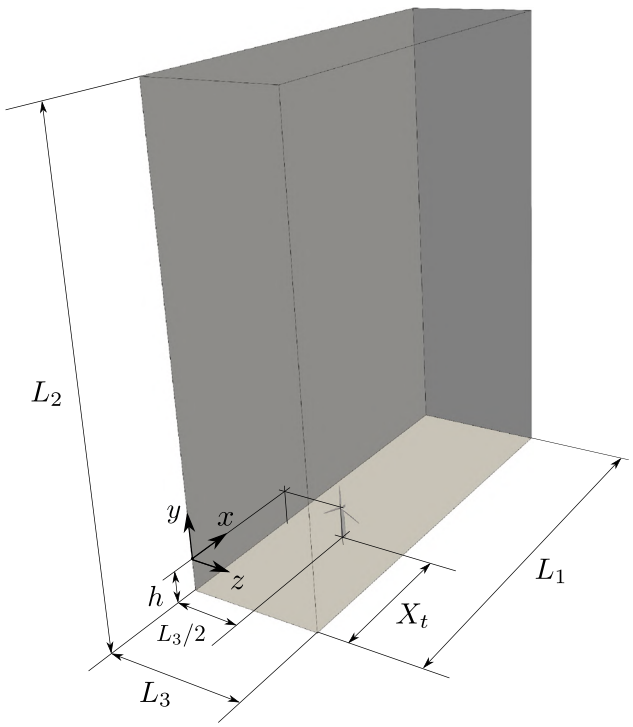

FIGURE 4 Fluid computational domain with the adopted nomenclature

According to previous works,[42] we use a number of modes $M = 15$ and a number of structural nodes $N = 80$ equally spaced along each blade.

The UA module adopts the model constants of the wind turbine's airfoils available from the reference database,[81] with tabulated airfoil data already corrected to include 3D rotational augmentation effects,[82,83] and empirical parameters already tuned to consider thick profiles too.[37]

Table 2 reports an outline of the simulations carried out. Each simulation run for approximately 60 revolutions after an initial transient (a period approximately equal to L_x/U, not considered in the evaluation of the statistics), at $Re = 8.5 \times 10^7$, and at constant Courant-Friedrichs-Lewy (CFL) number $CFL = 0.2$. The structural dynamics of all the coupled simulations has been initialised from a static equilibrium condition at rest (null deformation velocity). We considered eight sets of simulations including all the possible combinations of the different kinds of inflow, FSI coupling and aerodynamics modelling presented above. The aim of this simulation campaign is thus to discern the isolated effects and the combined influence of each of the considered aspects on the response of the utility-scale wind turbine under study.

4 | RESULTS

In the following, we consider the behaviour of the power and the thurst, of the aerodynamics loads, of the structural response and of the reactions. Then, we examine some of the variables introduced by the UA model, and finally, we analyse the fluid flow behaviour.

We indicate the time average with $\overline{\bullet}$, the phase average with $\langle \bullet \rangle$ and the average on the rotor area with $\langle \bullet \rangle_A$.

TABLE 2 Outline of the simulations carried out. Inflow can be uniform or sheared turbulent (ABL)

#	Name	Inflow	FSI	UA
1	U-ALM	Uniform	One-way	No
2	U-ALM/IV	Uniform	Two-way	No
3	U-ALM-UA	Uniform	One-way	Yes
4	U-ALM/IV-UA	Uniform	Two-way	Yes
5	ABL-ALM	ABL	One-way	No
6	ABL-ALM/IV	ABL	Two-way	No
7	ABL-ALM-UA	ABL	One-way	Yes
8	ABL-ALM/IV-UA	ABL	Two-way	Yes

Note: Classic ALM with rigid blades is used when one-way FSI is considered, whereas tabulated airfoil data are used when UA is not considered.
Abbreviations: ABL, actuator line model; ALM, actuator line model; FSI, fluid–structure interaction.

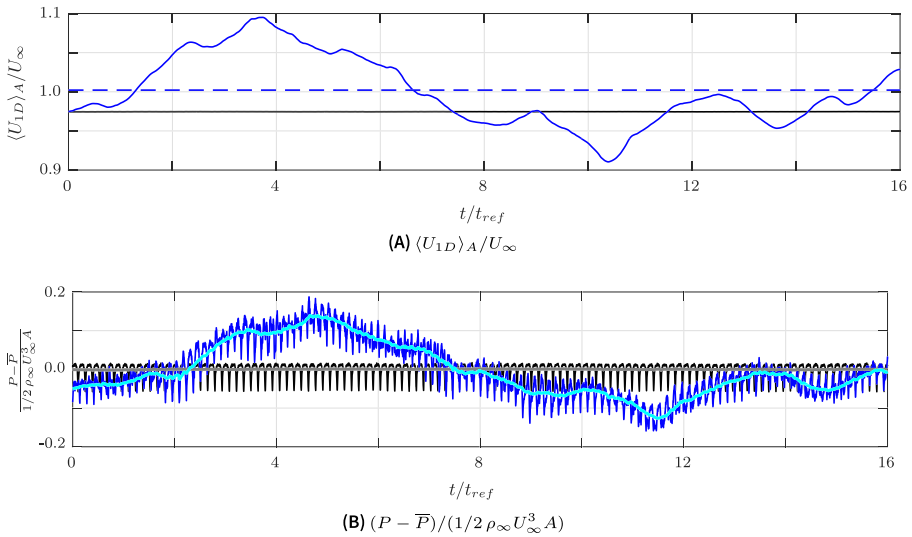

FIGURE 5 (A, B) Time history of the rotor-averaged streamwise velocity at one diameter from the hub $\langle U_{1D}\rangle_A/U$ and of the normalised power fluctuations for the U-actuator line model (ALM) and the atmospheric boundary layer (ABL)-ALM cases. The corresponding low-pass filtered signals are indicated in grey and cyan, respectively

4.1 | Power and thrust

At first, we compare the fluctuations relative to the mean value of the phase-averaged normalised power and thrust. Since power and thrust are obviously affected by the velocity of the flow impacting the wind turbine (see Figure 5, where $t_{ref} = D/U$), in the cases with turbulent ABL inflow, these quantities show large-scale fluctuations (related to the inflow turbulence as shown in Figure 5A), overlapped to local oscillations that are more associated with the tower shadowing (the high frequency fluctuations observable in Figure 5B), with the aeroelastic interaction and with the UA. To verify if the period considered for the averaging is sufficient to filter out the large-scale turbulent fluctuations, we high-pass filtered the power and thrust signals of the cases with turbulent inflow to remove the large-scale fluctuations, and we then derived the corresponding phase averages.* Given the large computational cost of the simulations, the time period considered is limited; however, the good agreement between the filtered and nonfiltered phase averages for the cases with turbulent ABL inflow (Figure 6) demonstrates that the period considered is sufficient to filter out the large scale fluctuations. Hence, we assume that it is reasonable to compare the phase-averaged results relative to the uniform and ABL cases.

From Figure 6, reporting the above presented fluctuations, we can see that the unsteady aerodynamics has a limited effect on power and thrust and thus that the local loads' fluctuations have a zero mean around the corresponding steady-state values and also that their distribution does not affect the integration of the loads along the blades' span. On the other hand, the introduction of the aeroelastic feedback generates the

*The generic filtered signal A^f is the subtraction from the original signal A of the low-pass filtered signal obtained by means of a 1-D digital FIR filter.[84]

oscillations centred approximately around $\Theta = 60^\circ$, 180° and 300°, already shown in Della Posta et al.[42] The shadowing effect experienced by the blades when passing in front of the tower triggers particularly the vibration of the structure, and the resulting aeroelastic response of the blade (in terms of deformation velocity, especially in the out-of-plane direction) induces load fluctuations that finally account for the fluctuations of the power and thrust after the drops due to tower shadowing.

The distribution of the phase-averaged coefficients differs from the cases with laminar, uniform inflow and those with turbulent, sheared inflow. Mainly three states can be identified in these coefficients: the tower shadowing dips ($\Theta = 30^\circ$, 150° and 270°, one of the blade is in front of the tower), the undisturbed top value (clearly visible in the one-way coupled cases, none of the blades is in front of the tower) and the vibration-induced peaks (between the tower shadowing dips, for the two-way coupled cases only). The cases with uniform inflow have sharp transitions between the first two aforementioned states (see highlighted regions in Figure 6), whereas the influence of mean wind shear and turbulence makes the transition between the different states smoother and the amplitude of the dips weaker, given the fact that the abrupt effect of the tower shadowing is mitigated by the presence of more significant turbulent fluctuations.

4.2 | Aerodynamic forces

Figure 7 reports the time average of the aerodynamic forces in the flapwise and edgewise direction, $\overline{F_2}$ and $\overline{F_3}$, respectively, and of the pitching moment, $\overline{M}$, along the blades' span. The distributions, consistent with Heinz,[58] show that the time average of the aerodynamic forces is the same for the same inflow. In other words, both FSI and UA preserve the mean loads, which thus can be estimated by one-way coupled simulations with classic sectional aerodynamics. A slight increase in the aerodynamic loads can be noticed for the case with ABL inflow, due—most likely—to a slightly higher mean velocity at the inlet. Moreover, the results confirm the capability of the UA model to recover the steady-state values of the averaged forces.

However, the standard deviation of the airloads along the blade in Figure 8 starts to unveil the differences in the data set. Although we were not able to provide a fair comparison for the same conditions as in the case of the time-averaged airloads, we proved the validity of our data by checking them against the distributions of the standard deviation along the blade for similar cases in Ehrich et al[85] and in Trigeaux et al,[65] obtaining satisfactory results. The cases using the UA model exhibit a relevant increase in the airloads variability in the first half of the blade, whereas the cases with two-way FSI coupling exhibit a slight reduction towards the tip, as shown in our previous works. These effects are dominant in the uniform inflow cases, where the root values can reach five—or even more—times the values towards the tip, while their importance is reduced in the simulations with ABL inflow. For the latter, even if the first half of the blade still presents larger standard deviations, these remains comparable with the tip values. Moreover, the structural feedback lowers the load variance towards the tip and slightly increases it towards the hub. This can be explained by looking at Figure 9, which reports the time average and the standard deviation of the AoA along the blade for the uniform and ABL inflow cases. Although the mean distribution of the AoA remains constant, with higher values at the root, the variability of the angle is higher throughout the span for the ABL inflow cases, more in the external half of the blade. As a result, in the cases with ABL inflow, the

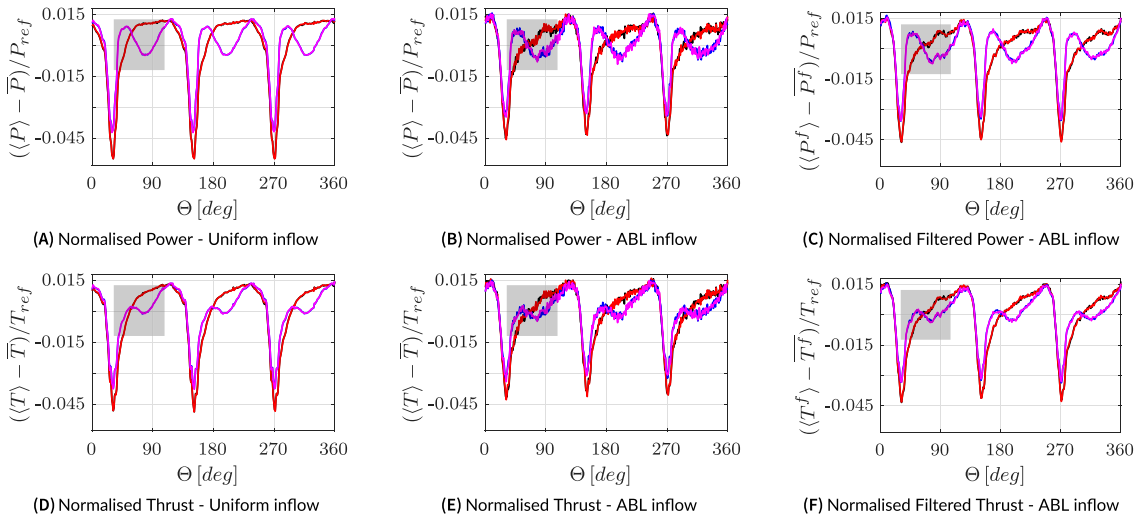

FIGURE 6 Phase-averaged fluctuations with respect to the mean value of the normalised power (top) and thrust (bottom) for the uniform-inflow cases (left), the atmospheric boundary layer (ABL)-inflow cases (centre), the filtered ABL-inflow cases (right). Colours from Table 2. The curves of the UA and corresponding non-UA cases are almost overlapped. $P_{ref} = 1/2\rho U^3 A$ and $T_{ref} = 1/2\rho U^2 A$. The transition regions are highlighted in grey

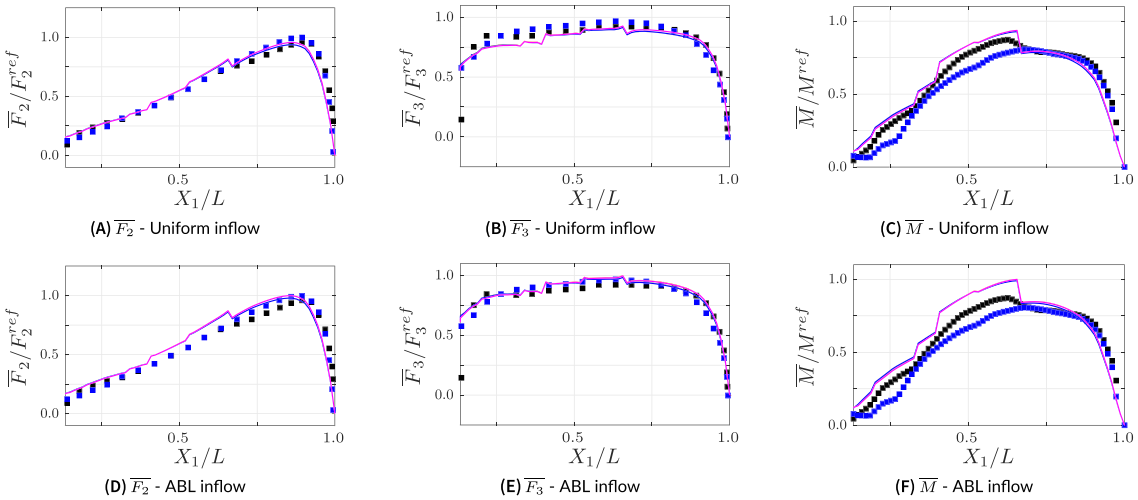

FIGURE 7 Time-averaged airloads per unit length along the blade span. Scatter data from Heinz:[58] ■ HAWC2 (blade element momentum [BEM]-based aeroelastic solver)[86] ■ HAWC2CFD (wall-resolved RANS-based aeroelastic solver).[58] Colours from Table 2. $F_2^{ref} = 6510\text{N/m}$, $F_3^{ref} = 669\text{N/m}$, $M^{ref} = 2760\text{N}$

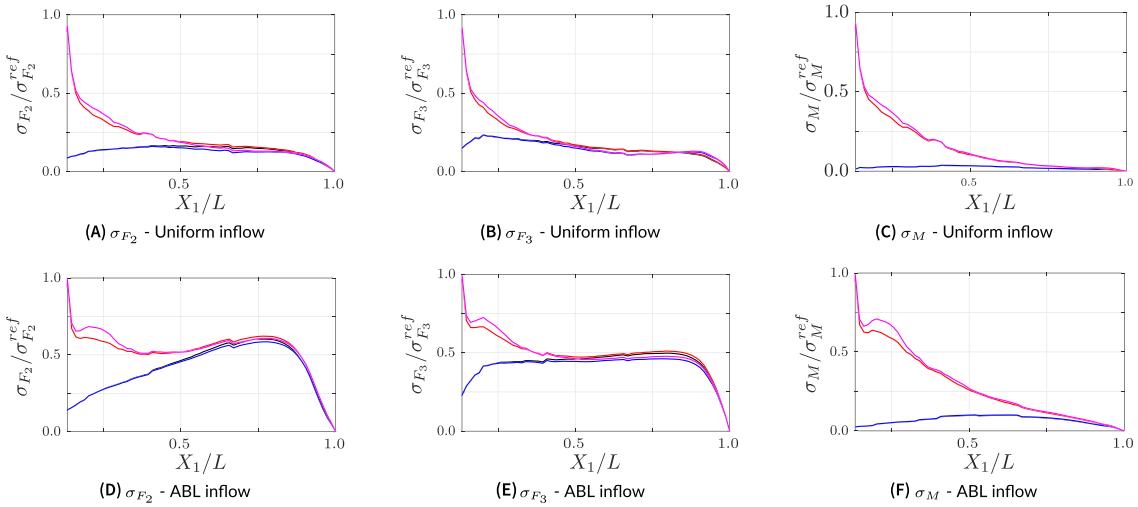

FIGURE 8 Standard deviation of the aerodynamic loads per unit length along the blade span. Colours from Table 2. $\sigma_{F_2}^{ref} = 1320\text{N/m}$, $\sigma_{F_3}^{ref} = 315\text{N/m}$, $\sigma_M^{ref} = 2430\text{N}$

variance of the loads increases in the tip portion so that the difference with the root is levelled, even if this is more related to the variability of the inflow than to effects related to UA.

From here, we can start to observe the division of the blades in two regions: the tip portion, mostly affected by the aeroelastic interaction, since here the deformations and the vibrations are more important, and the root portion, mostly affected by the UA effects. In fact, in the inner region of the blade, the fluctuations of α are substantial and the relative velocity is small. This makes the local flow highly unsteady and hence the airloads of the hub sections highly sensitive to the noncirculatory mechanisms and to other hysteresis phenomena strongly depending on $\dot{\alpha}$ (Equation (10)).

The pitching moment deserves careful scrutiny. The increase of the moment variability with the UA model is particularly high with both inflows. We will see that special attention must be devoted to the improvement of the description of the torsional moment. As a matter of fact, the modelling of the pitching moment dynamics is often disregarded in the literature, and also semi-empirical procedures used to determine it are not unambiguous compared to the descriptions of the normal force components, and thus their accuracy can be questioned.

To inspect the local airloads, Figure 10 reports the phase-averaged airloads in the cases with ABL inflow for two sections of the blade, respectively, at 25% (DU35_A17 airfoil) and 90% (NACA64_A17 airfoil). From the plots, the distinction of the two regions of influence is even clearer. For the root region, the faster and larger fluctuations of α with low incoming velocity induce sharp variations of the aerodynamic forces around

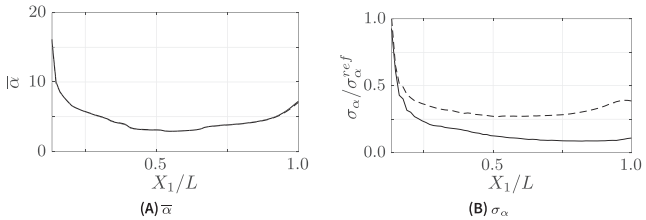

FIGURE 9 Time average (left) and standard deviation (right) of the Angle of Attack (AoA) along the blade span. – U-ALM, - - ABL-ALM. $\sigma_\alpha^{ref} = 2.76°$

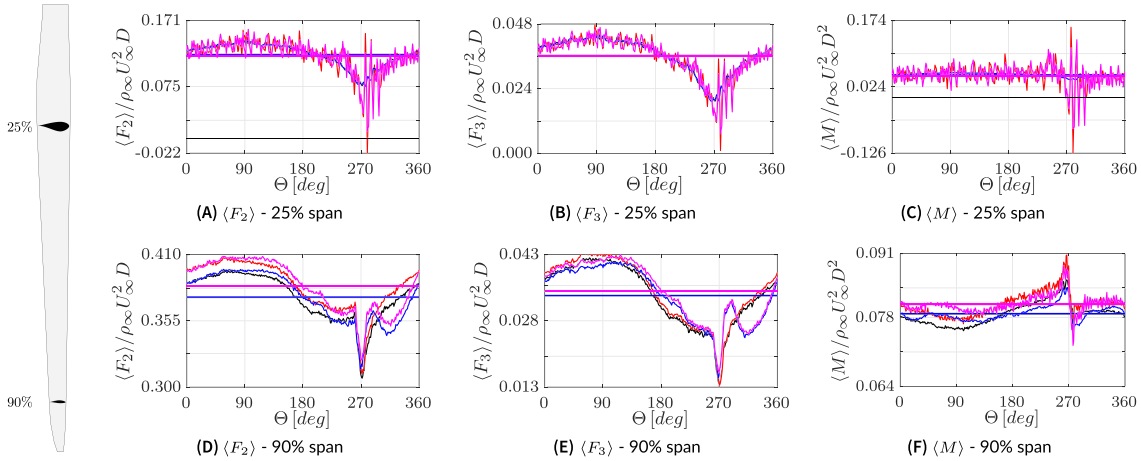

FIGURE 10 Phase-averaged airloads per unit length in the cases with atmospheric boundary layer (ABL) inflow (cases 5 to 8) at 25% (DU35_A17 airfoil, top row) and 90% (NACA64_A17, bottom row) of the blade length. The curves of the UA (non-UA) cases at 25% of the blade are almost overlapped. Colours from Table 2

the corresponding steady-state values obtained without UA. In particular, in correspondence of $\Theta = 270°$, the passage of the blade in front of the tower produces the largest variations of the loads. On the other hand, the effect of the structural vibrations close to the clumped hub is practically null, and thus, there is no relevant difference between the one-way and the two-way coupled cases. For the tip region, instead, the velocity is higher and the fluctuations of the AoA are smaller. The contributions from the UA model to the airloads are thus almost null, except a small increase in the mean values due also to small compressibility effects ($M^{max} \approx 0.2$ at 90% of the blade causes a 2% increase, in agreement with the Prandtl–Glauert correction). Conversely, the structural vibrations are here mostly important and affect the behaviour of the airloads, especially in the last quarter of revolution (see Figure 3). In the IV cases, it has been demonstrated[42] that the AoA and absolute value of the velocity are primarily influenced by the flapwise deformation velocity component v_2 of the structure. In particular, a positive increase of the flapwise deformation velocity v_2 induces a reduction of both the AoA and the velocity magnitude, which thus lowers the aerodynamic forces, and vice versa. Thus, when comparing the ALM and ALM/IV cases, the differences are determined by the behaviour of v_2: if v_2 increases, the aerodynamic loads in the ALM/IV case decrease compared with the ALM case; if v_2 decreases, the aerodynamic loads in the ALM/IV case increase compared with the ALM case. Moreover, given the fact that the most important load fluctuations due to UA are confined to the root region, which is less significant for the structural vibrations mainly taking place towards the external half of the blades, the ALM/IV and ALM/IV-UA cases do not show relevant differences, confirming that the effects of UA and FSI remain separated.

The local distribution of the phase-averaged pitching moment (Figure 10C) explicitly shows the very large and abrupt fluctuations deducible from the standard deviation. In fact, if small—but noticeable—fluctuations are present even at the tip, which do not affect the overall phase-averaged behaviour, high fluctuations, related to the noncirculatory normal force coefficient (see Section 4.5), alter completely the unsteady aerodynamic response, with severe overshoots compared with ALM and ALM/IV results with traditional tabulated airfoil data.

Figure 11 reports the comparison of the premultiplied spectra in logarithmic scale of the out-of-plane aerodynamic force component F_2 along the blade between the cases ABL-ALM/IV and ABL-ALM/IV-UA. Each vertical slice of the contour at a certain location shows the premultiplied spectrum of F_2 at that spanwise section. From the plots, we can recognise in both cases the trace of the loads' periodicity at the multiples of the rotor rotational frequency, given by the periodic passage of the blades in front of the tower and across the mean shear. Comparing the two cases, we can notice at first that the entire spectrum has larger values at high frequencies for the case with UA, because of the generalised increase in

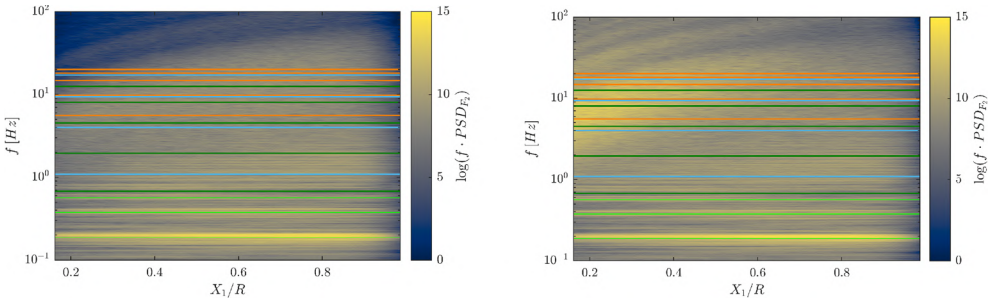

FIGURE 11 Premultiplied spectrum in logarithmic scale of the out-of-plane aerodynamic force component F_2 along the blade for the (A) atmospheric boundary layer (ABL)-ALM/IV and (B) ABL-actuator line model (ALM)/IV-UA cases. Horizontal lines indicate the frequencies corresponding to: first three multiples of the rotational frequency, first six flapwise modes, first four edgewise modes, first four torsional modes

variability of the loads throughout the blade. However, the most significant variations take places in the internal half of the blade, which sees an increased contribution throughout the high-frequency domain attributable to the rapid fluctuations of the noncirculatory loads in this region (see Section 4.5), which are related in turn to the dynamic history of the incoming flow and to the large time derivatives of the AoA.

Finally, Figure 12 shows the instantaneous and phase-averaged airloads as a function of the instantaneous AoA at 25% and 90% of the blade for the ABL-ALM/IV and ABL-ALM/IV-UA cases. The phase-averaged values are coloured on the basis of the corresponding azimuthal position of the blade. In this way, we can observe the aggregated hysteresis of the loads, including not only the hysteresis of the aerodynamic coefficients (see Section 4.5) but also the effect of the velocity fluctuations. The coloured phase averages show that the majority of the AoA variation is related to the tower shadowing and confined in the last quarter of revolution. The strong and sudden variation in AoA and velocity generates a hysteresis in the loads of both the sections. However, the larger hysteresis of the aerodynamic coefficients makes the variation of the loads at the root larger compared to the ones at the tip. In the end, the increased airloads variability, of the pitching moment in particular, is visible from the increased area covered by the instantaneous airloads in grey.

4.3 | Structural dynamics

Figure 13 shows the phase average of the flapwise, edgewise and torsional components of the displacement and of the deformation velocity at the blade's tip, for the cases with ABL inflow only. We can see that the FSI coupling has a major impact on the flapwise and torsional components, confirming the existence of a flapwise damping mechanism, whereas it has a practically negligible effect on the edgewise component, dominated by the sinusoidal weight force on the blade. As explained in Della Posta et al,[42] an increase in v_2 reduces the AoA and the relative velocity magnitude, which finally cause a reduction of the aerodynamic forces that were originating the v_2 increase itself, and vice versa. As a result, the contribution of the flapwise structural dynamics in Equation (7) accounts for the damping of the first structural mode (essentially a flapwise bending mode with a mild torsional influence) observable in the tip structural response in Figure 13 and in the premultiplied power spectral density (PSD) of the tip flapwise deformation velocity in Figure 14 for the cases with two-way FSI coupling. The $\langle v_2 \rangle$ fluctuations, mostly triggered by the passage of the blade in front of the tower, reach values that are comparable with the upstream fluid velocity in the last quadrant and thus influence largely the definition of the local aerodynamic forces. On the other hand, the smaller variation of the AoA and the larger importance of the structural vibrations towards the free tip of the long blades make the effect of UA at the tip practically negligible. However, if we look at the premultiplied spectrum in Figure 14, we can see that the UA cases have relevant energy peaks corresponding to the flapwise natural modes of the structure at higher frequencies, $f > 10$Hz.[†] The physical explanation for these peaks is shown in Figure 15, which reports the comparison of the time history of the first six flapwise modal loads e_i of the cases with ABL inflow during a rotor revolution. The modal load e_i is given by the projection of the forces on the structure onto the i-th mode of the blade. The increased amplitude of the last modal loads proves that the important high-frequency load fluctuations close to the hub, particularly induced by the UA of the normal force (as shown in Figure 11), trigger the higher-frequency bending modes, which are more influenced by the load distribution also in the region close to the clamped end.

[†]The difference in the flapwise motion is also visible from Video 1 in the additional material, where the time animation of the flapwise dynamics is compared between the ABL-ALM/IV (first row) and the ABL-ALM/IV-UA cases (second row). We reported the flapwise dynamics from the first three flapwise modes in the first three columns, the flapwise dynamics from all the other modes in the fourth column and the evolution of the total flapwise displacement all over the blade in the fifth column.

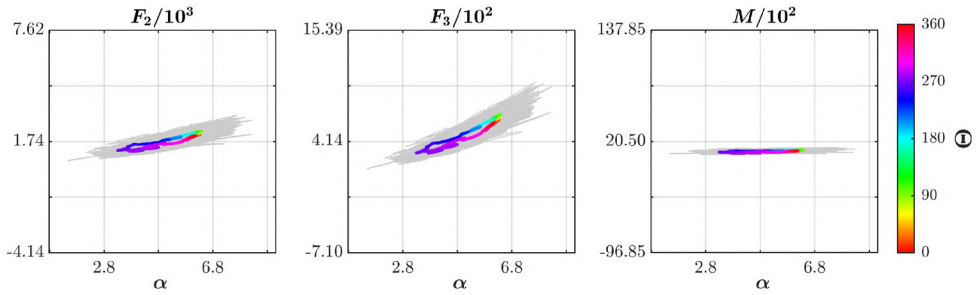

(A) Airloads at 25% span - ABL-ALM/IV case

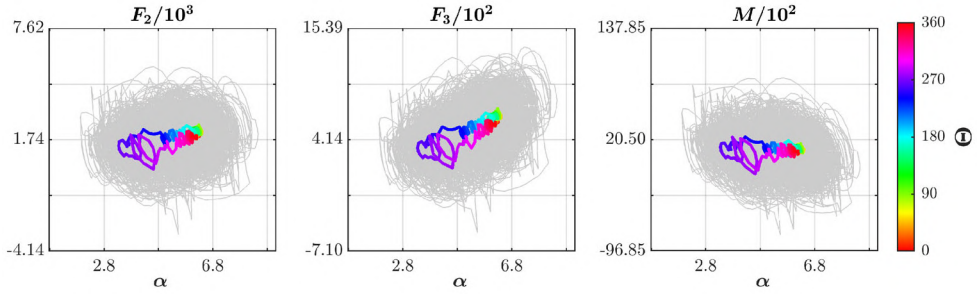

(B) Airloads at 25% span - ABL-ALM/IV-UA case

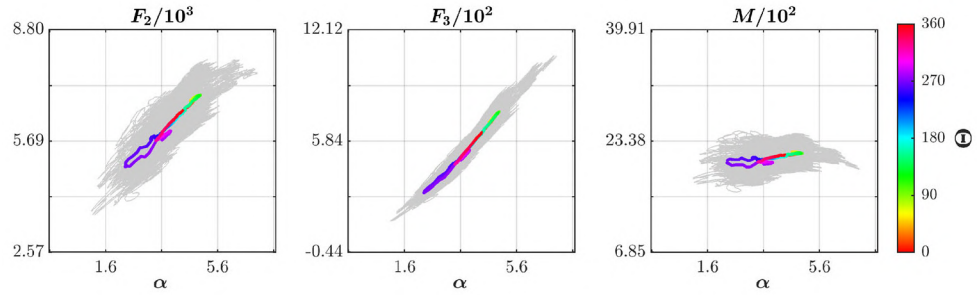

(C) Airloads at 90% span - ABL-ALM/IV case

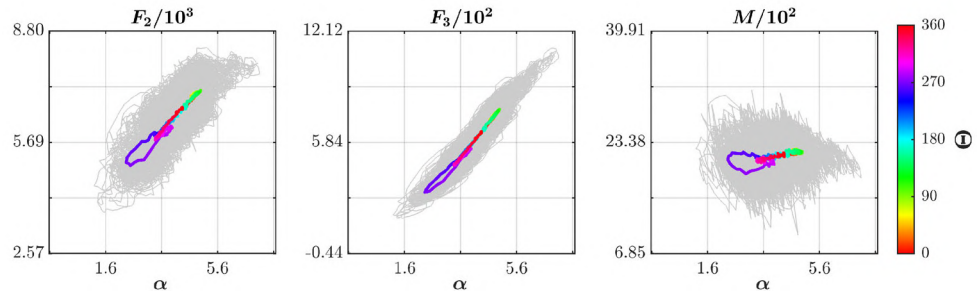

(D) Airloads at 90% span - ABL-ALM/IV-UA case

FIGURE 12 Instantaneous and phase-averaged airloads per unit length as a function of the Angle of Attack (AoA) in the cases with atmospheric boundary layer (ABL) inflow (cases 6 and 8) at 25% and 90% of the blade span. The colormap indicates the azimuthal angle in the phase average

Concerning the fluctuations of the unsteady pitching moment, even if their variation is large, since the blades under study are particularly stiff torsionally,[14] the increased fluctuations at frequencies potentially forcing the torsional structural modes (first torsional mode at $f \approx 5.58$Hz) do not affect dramatically the overall dynamics of θ_1. As a consequence, also, the indirect effect of the torsion on the flapwise motion, due to the eventual flexo-torsional coupling in the blade's structure, is rather small, and so we are confident that the results of our simulations are not compromised by the possible uncertainties in the pitching moment UA model. However, care must be taken, since we can see from Figure 14 that the increased fluctuations due to the UA model in the ALM/IV-UA cases start to reinforce the high-frequency structural response in general. In this way, torsional modes may also be activated, and even if they do not enter directly in the definition of the AoA in the FSI coupling considered in this work, they still may have a nonnegligible flexural component sensed in Equation (7).

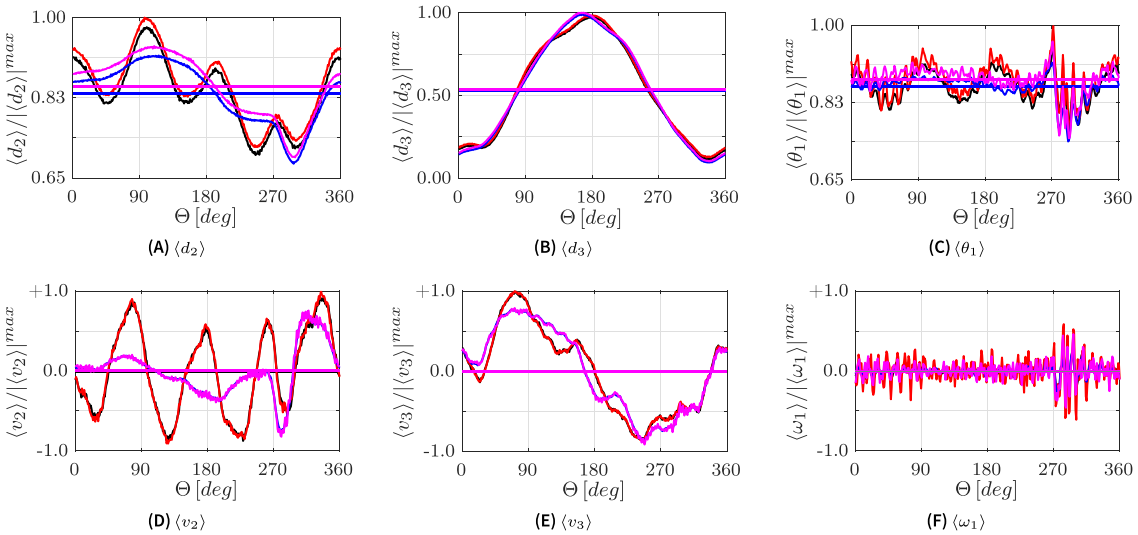

FIGURE 13 Phase-averaged flapwise (left), edgewise (centre), and torsional (right) components of the displacement (top) and corresponding components of the deformation velocity (bottom) at the blade tip for the cases with atmospheric boundary layer (ABL) inflow only (cases 5 to 8). Colours from Table 2. $|d_2|^{max} = 5.96$m, $|d_3|^{max} = 1.08$m, $|\theta_1|^{max} = 2.89$deg, $|v_2|^{max} = 2.45$m/s, $|v_3|^{max} = 0.789$m/s, $|\omega_1|^{max} = 18.6°$/s

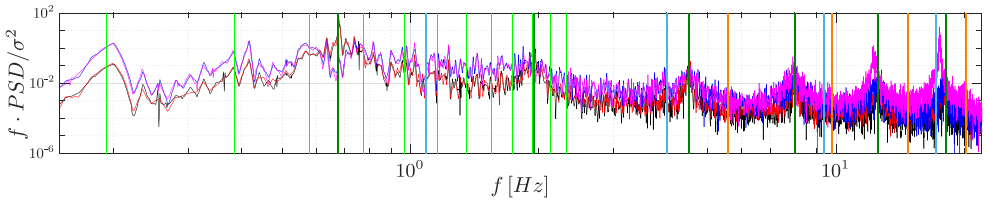

FIGURE 14 Premultiplied power spectral density of the flapwise deformation velocity at the tip, normalised by the corresponding variance (cases 5 to 8). Colours from Table 2. Vertical lines indicate the frequencies corresponding to: first 12 multiples of the rotational frequency, first 6 flapwise modes, first 4 edgewise modes, first 4 torsional modes. The last two modes reported are flexo-torsional modes with a dominant flapwise nature in the first case and a dominant torsional nature in the second case

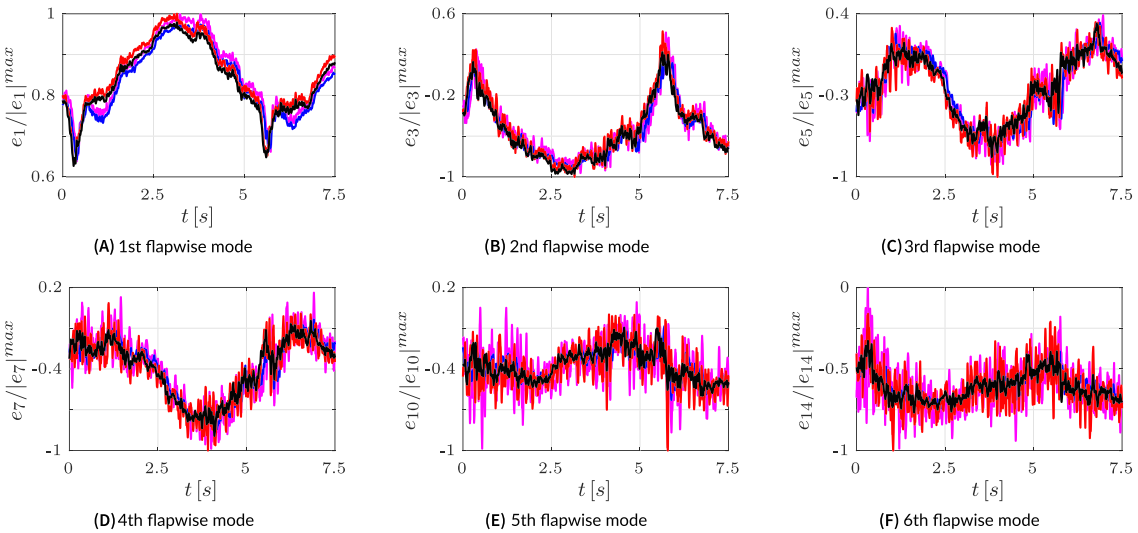

FIGURE 15 Time history for approximately one revolution of the modal loads e_i of the first six flapwise modes. Cases 5 to 8, colours from Table 2. $|e_1|^{max} = 3062$N, $|e_2|^{max} = 384$N, $|e_3|^{max} = 295$N, $|e_4|^{max} = 374$N, $|e_5|^{max} = 302$N, $|e_6|^{max} = 334$N

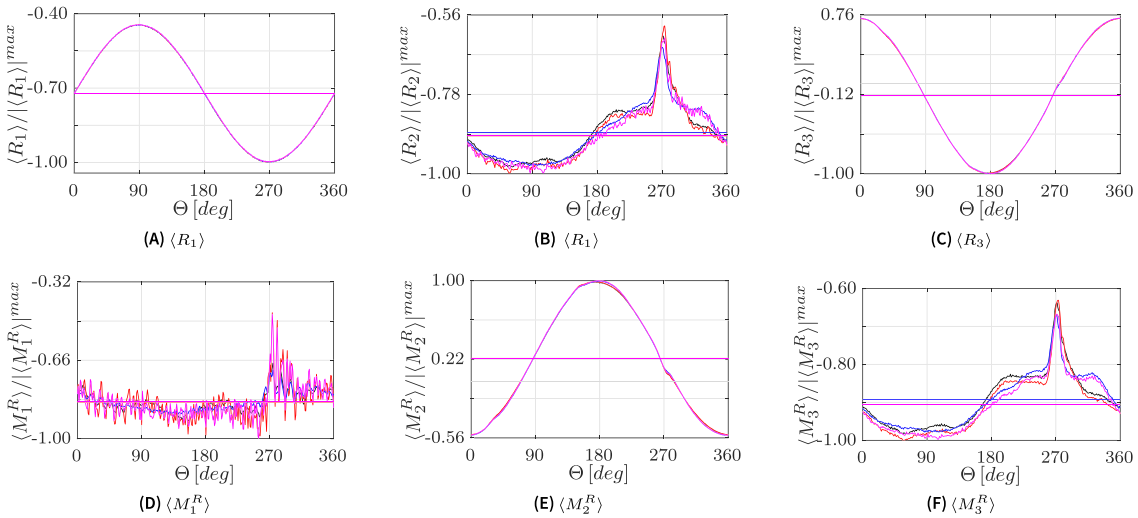

FIGURE 16 Phase-averaged force and moment components of the root reaction for the cases with ABL inflow only (cases 5 to 8). Colours from Table 2. $|R_1|^{max} = 6.24 \cdot 10^5$N, $|R_2|^{max} = 2.41 \cdot 10^5$N, $|R_3|^{max} = 2.00 \cdot 10^5$N, $|M_1^R|^{max} = 1.13 \cdot 10^5$N·m, $|M_2^R|^{max} = 4.60 \cdot 10^6$N·m, $|M_3^R|^{max} = 9.54 \cdot 10^6$N·m

4.4 | Reactions

Figure 16 shows the phase average of the six components of the reaction at the blade's root for the cases with ABL inflow. We indicate with R_1, R_2 and R_3 the axial, flapwise and edgewise components of the reaction force respectively, and with M_1^R, M_2^R and M_3^R the torsional, edgewise and flapwise reaction moment components, respectively.

As expected, R_3 and M_2^R are mostly sinusoidal and determined by the gravitational force that is maximum at the multiples of $\Theta = 180°$. The axial component R_1 instead is completely determined by the gravity and the centrifugal force. On the other hand, the flapwise and torsional components show the influence of the structural vibrations, which is dominant around the main source of structural unsteadiness, that is, the tower. Moreover, UA introduces additional oscillations affecting the local behaviour. The amplitude of these contributions is larger for the torsional root moment, which experiences the large variability of the pitching moment.

To enrich the analysis of the response of the wind turbine, we compare the fatigue properties from the root reactions. We thus estimate the widely used damage equivalent load (DEL),[87] which represents the amplitude of the single constant-rate alternating load producing the same total damage of the real load spectrum. To evaluate the DELs for the root components of each case, we used the post-processing tool MCrunch.[88]

Tables 3 and 4 report the DELs for the U-ALM and ABL-ALM reference cases and the percentage differences between each case and the relative reference one. The results confirm previous findings[42] regarding the overprediction of the load fluctuations by using one-way coupled simulations. In particular, we demonstrated how the aerodynamic damping due to FSI coupling limits the flapwise and torsional vibrations of the blade and thus reduces by almost 10%–20% the DELs of the corresponding components. By comparing the results of the cases with uniform and ABL inflows, turbulence and mean shear increase by almost the double the equivalent airloads of the uniform inflow cases. Meanwhile, the turbulent ABL inflow limits the differences between the one- and two-way coupled cases, which confirms that turbulence mitigates the impact of the structural vibrations on the aerodynamics. However, torsional root reactions do not seem to be affected by the different coupling conditions, with only small differences between the uniform and ABL inflow cases.

On the contrary, the introduction of the UA model has an opposite effect on the equivalent airloads: the additional fluctuations produced by the airloads hysteresis increase considerably all the DELs, especially the flapwise components affected by the hysteresis of C_n.

As a result of the two counteracting effects, the DELs of the IV-UA cases have an intermediate shift with respect to the ALM cases. In particular, they show that the increase due to the UA dominates over the decrease due to the aeroelastic coupling for R_2, while the contrary happens for M_3^R. This disagreement is actually coherent with the distribution of the forces and with the different regions of influence along the blade. In fact, the force component is only given by a thorough integration of the force along the span, which makes no distinction concerning where the sectional force is applied. On the other hand, the moment depends on where the sectional force is applied and privileges the forces towards the tip. As a consequence, for M_3^R, the diminishing effect of the tip aeroelastic coupling prevails over the increasing effect of the root UA.

TABLE 3 Damage equivalent load (DEL) of the reaction components: uniform inflow

DEL	$R_1[N]$	$R_2[N]$	$R_3[N]$	$M_1^R[N\cdot m]$	$M_2^R[N\cdot m]$	$M_3^R[N\cdot m]$
U-ALM	146.0	24.73	145.9	12.01	2988	942.0
$\Delta R_i\%$	$\Delta R_1\%$	$\Delta R_2\%$	$\Delta R_3\%$	$\Delta M_1^R\%$	$\Delta M_2^R\%$	$\Delta M_3^R\%$
U-ALM-UA	0.00%	+24.73 %	+0.34 %	+268.71 %	+0.27 %	+8.28 %
U-ALM/IV	−0.03 %	−20.75 %	+0.10 %	−21.81 %	+0.22 %	−24.58 %
U-ALM/IV-UA	0.00%	+14.14 %	+0.58 %	+230.34 %	+0.49 %	−15.13 %

Note: The DELs of the baseline U-ALM case are reported together with the percentage differences for the other cases. The percentage difference for the generic root reaction component R_i is defined as $\Delta R_i\% = 100\cdot(DEL_{R_i} - DEL_{R_i}^{ALM})/DEL_{R_i}^{ALM}$, where DEL_{R_i} is the DEL of the i-th root component of the case considered, and $DEL_{R_i}^{ALM}$ is that of the corresponding one-way coupled case without unsteady aerodynamics and with the same inflow (U-ALM).
Abbreviation: ALM,actuator line model.

TABLE 4 Damage equivalent load of the reaction components: ABL inflow

DEL	$R_1[N]$	$R_2[N]$	$R_3[N]$	$M_1^R[N\cdot m]$	$M_2^R[N\cdot m]$	$M_3^R[N\cdot m]$
ABL-ALM	152.0	47.95	146.0	23.98	2992	1840
$\Delta R_i\%$	$\Delta R_1\%$	$\Delta R_2\%$	$\Delta R_3\%$	$\Delta M_1^R\%$	$\Delta M_2^R\%$	$\Delta M_3^R\%$
ABL-ALM-UA	−0.07 %	+15.11 %	+0.48 %	+193.58 %	+0.25 %	+7.09 %
ABL-ALM/IV	+0.00 %	−11.27 %	+0.41 %	−25.35 %	+0.70 %	−13.56 %
ABL-ALM/IV-UA	−0.10 %	+7.81 %	+1.44 %	+196.50 %	+1.19 %	−6.39 %

Note: As in Table 3, but the baseline is the ABL-ALM case.
Abbreviations: ABL, atmospheric boundary layer; ALM, actuator line model.

4.5 | UA variables

In this section, we examine the phase average of the various definitions of the AoA, the delayed separation point and the contributions to the attached normal force component introduced by the UA model for two sections at 25% and 90% of the blade, respectively.

Figure 17 reports the comparison between the ABL-ALM/UA and the ABL-ALM/IV-UA cases at 25% and 90% of the blade. The curves in Figure 17A confirm that the AoA is not affected by the structural vibrations close to the root of the blade, while the curves in Figure 17D show the sinusoidal variation due to the mean shear and confirm the effect of the aeroelastic interaction, especially in the last quadrant. Furthermore, it is visible that in the first half of the blade, the UA model introduces a noticeable delay between the geometric AoA $\langle\alpha\rangle$, the effective AoA $\langle\alpha_f\rangle$ and even more in the chordwise-effective AoA $\langle\alpha''\rangle$. It is also possible to see that, given the small time in which the blade covers the azimuthal region around the tower, large derivatives of the AoA take place close to the root at low velocities, suggesting the relevant role of noncirculatory components here.

The decrease of the AoA shown in the tower region accounts for the gradual increase of the separation point function $\langle f\rangle$ and of its delayed estimation $\langle f''\rangle$, which is visible in Figure 17B. Close to the hub, the flow on the airfoil is always separated, with approximately 10% of the chord always covered by separated flow, and there is a relevant delay between $\langle f\rangle$ and $\langle f''\rangle$. On the other hand, towards the tip of the blade, the flow is almost fully attached, and the main source of motion to the separation point becomes the sinusoidal fluctuations imposed by the wind shear and the aeroelastic modifications. Moreover, the delay between $\langle f\rangle$ and $\langle f''\rangle$ is almost null.

The different response of the separation point to a qualitatively similar variation of the AoA throughout the rotor revolution depends mostly on the different $f-\alpha$ curves of the airfoils of the two regions. In particular, Figure 18 shows that the AoA fluctuations close to the tip take place near the sharp knee between the flat and steep regions of the separation point curve, while close to the hub they take place in a region with approximately uniform slope. Indeed, the airfoils closer to the tip are thinner and have a broader linear attached region in the aerodynamic polar, which makes the f curve flat on top for a broader region and then suddenly steep. Thick profiles in the first half of the blade, and especially really close to the root, have instead a more limited linear portion, since flow tends to separate soon and progressively, and thus their f curves have smoother knee on top. As a result, even assuming the same history of the AoA, the response $f(\alpha(t))$ is different.

Figure 17C–F report the comparison of the contributions to the potential normal force coefficient. The differences in C_n^{pot} for the different cases are actually the origin of the differences in the complete airfoil coefficients, since the contribution from the LEV is almost null (not shown for brevity). We can immediately notice that the aeroelastic coupling has only an effect on the circulatory component of the tip profile, since it influences directly the modification of the geometric AoA. On the other hand, the noncirculatory component is insignificant at the tip, while being

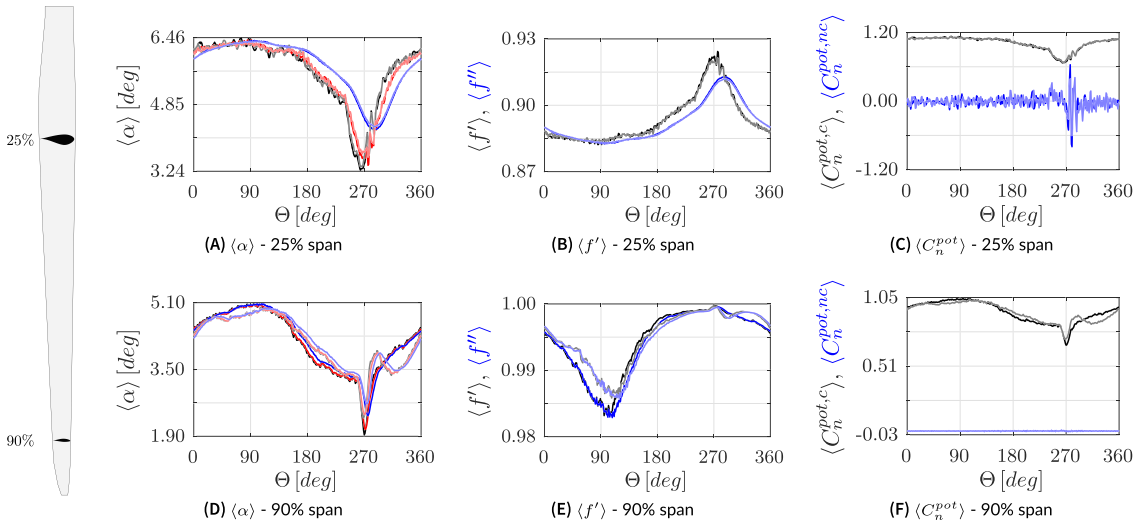

FIGURE 17 Phase average of some variables of the UA model for the atmospheric boundary layer (ABL)-actuator line model (ALM)-UA case and the ABL-ALM/IV-UA at 25% (top) and 90% (bottom) of the blade span (shown on the left): various definitions of the Angle of Attack (AoA), delayed separation point, contributions to the attached normal force coefficient. Full lines are referred to the ABL-ALM-UA case, shaded lines to the ABL-ALM/IV-UA case. In the AoA plots, we report the instantaneous geometric AoA α, the effective AoA α_f and the chordwise-effective AoA α''

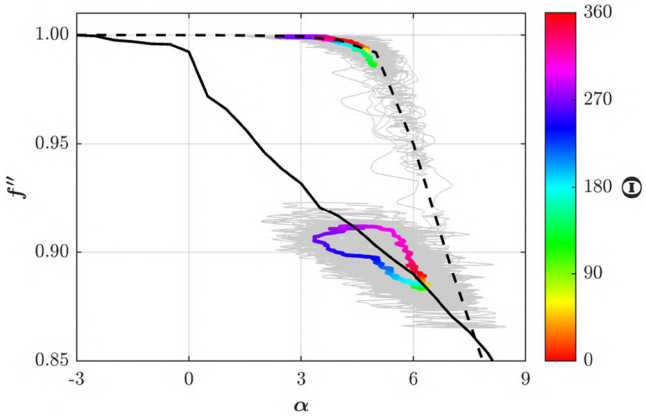

FIGURE 18 Hysteresis of the separation point at 25% (DU35_A17 $f-\alpha$ curve, –) and 90% (NACA64_A17 $f-\alpha$ curve, - -): instantaneous and phase-averaged f'' as a function of the Angle of Attack (AoA) in the atmospheric boundary layer (ABL)-actuator line model (ALM)/IV-UA case. The colormap indicates the azimuthal angle in the phase average

comparable with the circulatory component at the root. Here, where the variability of the AoA and the chord are larger, and the flow velocity is smaller (q at the root can be even 6 times higher than at the tip), the oscillations of $C_n^{pot,nc}$ can even overshadow the main $C_n^{pot,c}$ especially close the tower passage, which remains the main source of unsteadiness for both the structure and the aerodynamics.

In order to better identify the two different conceptual regions in which the blade can be split (tip region dominated by FSI, root region dominated by UA), we report in Figure 19 the fraction of time with respect to the total one T_{nc}/T for which the noncirculatory part $C_n^{pot,nc}$ accounts for more than 50% of the whole normal force component C_n at each section of the blade, for the UA cases with ABL inflow. From this figure, we can observe that the division between the two regions of influence is actually rather sharp, since only the inner 25% of the blade has a significant contribution from the noncirculatory loads dominating the UA. As a result, there is certainly a smooth transition region, but the conceptual split between the two areas of influence is also quantitatively representative.

In the end, similar to the complete airloads in Figure 12, Figure 20 reports the phase-averaged and instantaneous hysteresis of the airload coefficients only for the ABL-ALM/IV-UA case at 25% and 90% of the blade. The coefficients oscillate around the steady-state values, confirming the ability of our UA model to recover in the average the usual tabulated values, and attest the main source of variation around $\Theta = 270°$. Besides noting generally the different extent of the hysteresis at the two sections, we highlight the narrower hysteresis of C_c related to the limited

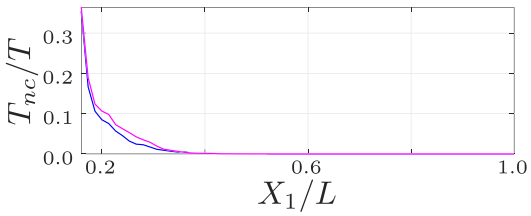

FIGURE 19 Fraction of time with respect to the total one T_{nc}/T for which the noncirculatory part $C_n^{pot,nc}$ accounts for more than 50% of the whole normal force component C_n at each section of the blade, for the atmospheric boundary layer (ABL)-actuator line model (ALM)-UA and ABL-ALM/IV-UA cases (cases 7 and 8)

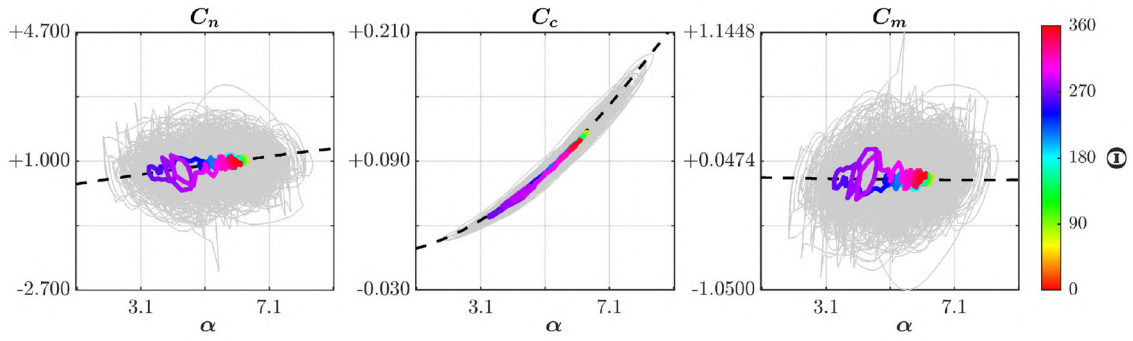

(A) Airloads at 25% span - ABL-ALM/IV-UA case

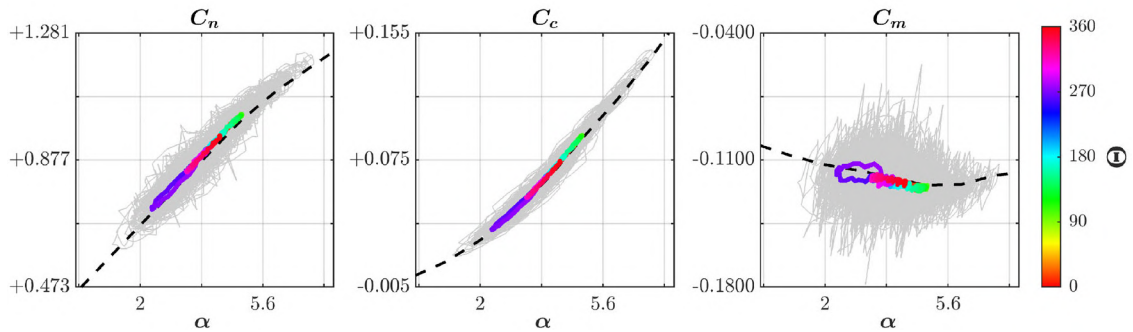

(B) Airloads at 90% span - ABL-ALM/IV-UA case

FIGURE 20 Instantaneous and phase-averaged airload coefficients as a function of the Angle of Attack (AoA) in case atmospheric boundary layer (ABL)-actuator line model (ALM)/IV-UA at 25% (top) and 90% (bottom). The colormap indicates the azimuthal angle in the phase average

variability of the circulatory component of C_n, from which C_c mainly depends (Equation (14b)). Finally, we observe the very large hysteresis of C_m. For this component, the noncirculatory component remains significant also at the tip and far larger than the small circulatory part typical for small angles of attack.

4.6 | Fluid flow

In general, we have noticed that the mean fluid flow is not affected significantly by the aeroelastic coupling and the UA. For this reason, we present in the following only a quick comparison between U-ALM and ABL-ALM cases and an overview of the flow topology in the rotor region influencing the response of the blades.

Figure 21 compares the mean turbulent kinetic energy (TKE) for the U-ALM and the ABL-ALM cases on vertical and horizontal slices through the hub. The contours show that the tower introduces an asymmetry in the wake, with a recirculation region just behind the tower and the nacelle. Moreover, the increased mixing induced by the turbulent ABL inflow stimulates a more intense activity behind the wind turbine, promoting a faster wake recovery, as observable also from the rotor-averaged velocity along the streamwise axis in Figure 22. Small differences in the organisation of the flow just behind the tower and the nacelle can also be noticed: the imposed mean shear reduces the extent of the recirculating

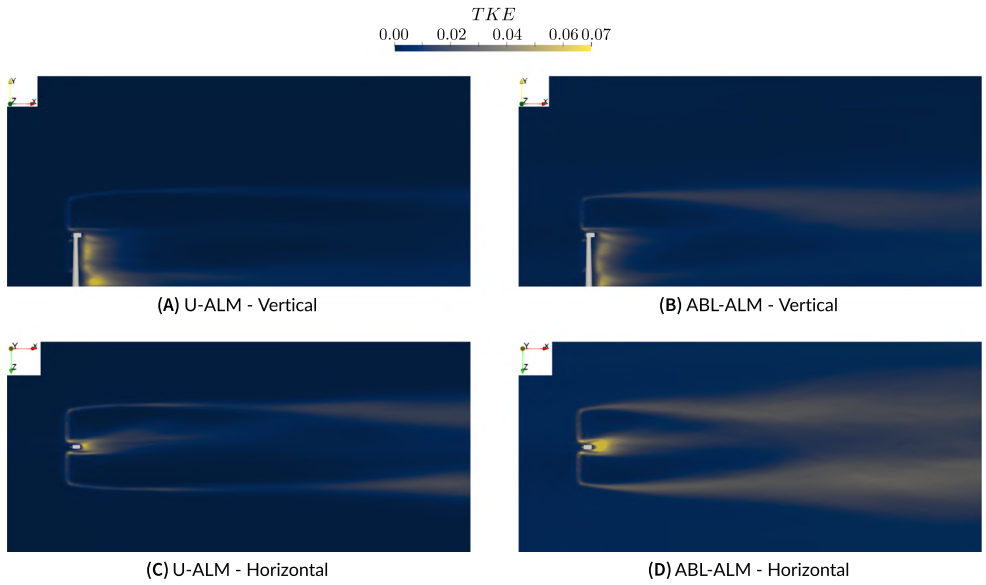

FIGURE 21 Time-averaged turbulent kinetic energy on vertical (top) and horizontal (bottom) slices through the hub. U-actuator line model (ALM) (left), atmospheric boundary layer (ABL)-ALM (right)

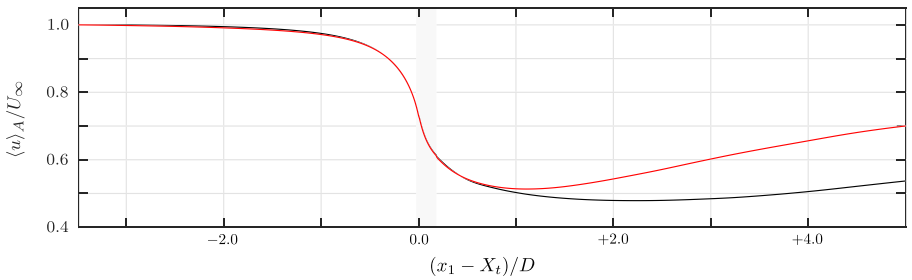

FIGURE 22 Rotor-averaged velocity along $(x_1 - X_t)/D$. atmospheric boundary layer (ABL)-actuator line model (ALM) curve is scaled by the value of the rotor-averaged velocity at the inlet, which is slightly larger than U. The region occupied by the wind turbine is indicated in gray. U-ALM –, ABL-ALM –

region at the feet of the tower and enhances the one behind the nacelle. In order to validate the rates of recovery obtained, we have estimated the optimal parameters A and n able to describe the velocity deficit through the power law expression $\Delta\langle u \rangle_A / U = A(D/x)^n$ in the far field (at least $(x_1 - X_t)/D > 3$ to avoid the effect of the tower and the nacelle[89]). Even if the domain used is rather short to estimate properly the decay of the velocity deficit in the far field (especially for the cases with uniform inflow), the values obtained ($A = 0.78$ and $n = 0.59$ for the cases with ABL inflow) agree adequately with those obtained by Aitken et al[90] through fitting of a large data set of experimental measurements ($A = 0.56$ and $n = 0.57$).

Figure 23 reports instead the time-averaged velocity components for the U-ALM case on a vertical slice in correspondence of the rotor, with arrows indicating the velocity in the plane. The figures spotlight how the 3D and complex interaction between the disc blockage, the tower shadowing and the swirl induced by the blades break the axisymmetry of the flow in the proximity of the rotor, affecting the local fluid dynamics that determines the aerodynamic loads on the blades. In particular, the interaction between the tower and the swirled flow induced by the rotor generates a mean flow slightly skewed towards the left ($z < z_t$) for a counterclockwise-rotating rotor. The obstruction due to the asymmetric recirculation region behind the tower induces the streamwise velocity to slightly increase on the left and and vice versa on the right. Moreover, the assumed conical shape of the tower generates a decrease of the flow velocity that is not homogeneous in the vertical direction. Thus, the lower part of the blades feels more the tower shadowing and the imposed flow deceleration.

As a result, we can divide the flow in the proximity of the rotor into four different regions:

- Close to the terrain, the tower is not hidden by the rotor and the flow is deviated symmetrically in the lateral directions.
- In the bottom tip region, the enlargement of the stream tube impacting the rotor induces a radial flow component. The flow is determined by the combination of this component with the tower shadowing, whose effect is maximum here. From here, we can observe the asymmetry of

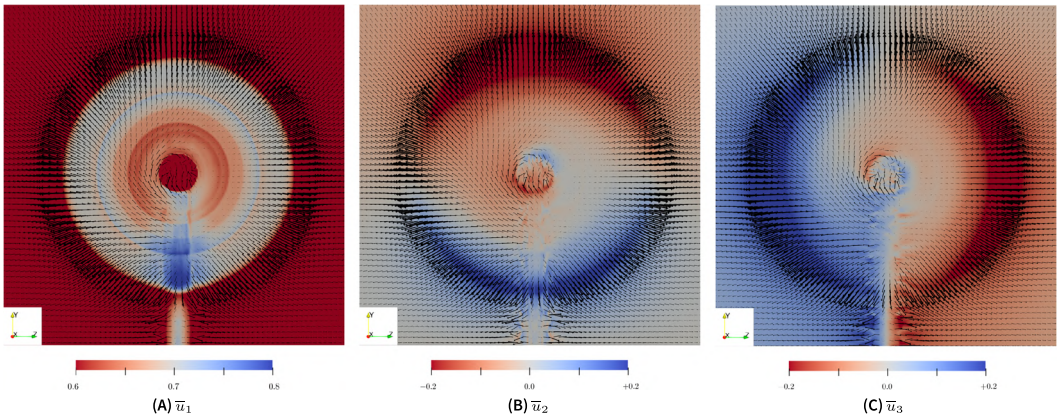

FIGURE 23 Time-averaged streamwise (left), vertical (centre), spanwise (right) velocity components on a vertical plane in correspondence of the rotor for the U-actuator line model (ALM) case, with arrows indicating the velocity in the plane

the flow towards the left side of the turbine: while the fluid particles on the left do not find any obstacle in following the imposed clockwise swirl, the fluid particles on the right are blocked by the tower and thus forced to flow more radially, towards the terrain.

- After a region of transition, close to the root, the tower shadowing is less evident and the flow is dominated by the blades' swirl at the left of the tower (the rotor rotates in counterclockwise direction). At the right, the decelerated flow remains mainly streamwise and progressively goes radially proceeding towards the tip of the blade, because of the increase in the stream tube area. Future works will also consider the presence of the hub in the geometry of the immersed body, whose lack in this case accounts for the overestimated velocities in the central region.
- Above the nacelle, where there is no tower shadowing, the left and right flows merge together producing a flow that—in the plane—gradually tends to follow the opening of the stream tube towards the tip and the rotation imposed by the blades.

5 | CONCLUSIONS

Despite the potential role of UA phenomena for increasingly large wind turbines, their effects on the local aerodynamics have been scarcely investigated with the purpose of improving the modelling of HAWTs in high-fidelity CFD frameworks that simplify the blades' representation to avoid heavy wall-resolved approaches. In addition to proven usefulness in engineering methods like BEM,[91] the adoption of UA models to estimate the airloads' coefficients has the potential to complete the description of the local aerodynamics also in those CFD methodologies that do not use the sufficient resolution to solve explicitly the blade boundary layer. A case in point is the ALM and the other GADMs, which typically use only steady tabulated airfoil data from wind tunnel measurements to evaluate the local aerodynamic forces.

For this reason, in this work, we examined the effects of an UA model for the evaluation of the sectional aerodynamic forces in an LES-based FSI solver for wind energy. A semi-empirical Beddoes–Leishman model has been implemented to evaluate dynamically the aerodynamic coefficients of the blade's airfoil in the ALM of our LES solver, instead of using fixed tabulated airfoil data. In particular, we considered a set of simulations of the baseline onshore NREL 5 MW HAWT assessing the global behaviour of such a utility-scale wind turbine with uniform, laminar or sheared, turbulent inflows, with and without the UA model and for one- and two-way aeroelastic coupling.

Our results show that the effects of both UA and FSI are not directly visible in the time-averaged behaviour but rather more in the variability of all the aerodynamic and structural quantities. For fully coupled simulations, we observed that the blade is divided into two regions of influence: the tip region, mainly influenced by important flapwise vibrations affecting the local AoA, and the root region, mainly influenced by significant oscillations of the AoA (larger than in the rest of the blade; see Figure 9) at low fluid velocity that generate large noncirculatory contributions to the airfoil coefficients. Inflow turbulence mitigates the differences between the two regions and increases the variability of the loads throughout the blade. However, if one avoids considering the corrections to the local aerodynamics due to UA, even a high-fidelity fluid solver with ALM would underestimate the loads' variability severely, affecting the evaluation of the unsteady response of the wind turbine.

Even for the cases with turbulent ABL inflow, the dominant source of aerodynamic and structural unsteadiness is confirmed to be the presence of the tower, which is thus a critical element to be considered to properly estimate the overall wind turbine behaviour. Tower shadowing causes a sudden variation of the flow that curtails the airloads, promotes the flapwise and torsional structural vibration, triggers the surge of added mass effects thus amplifying the airload hysteresis, and causes a mean deflection in wake flow.

Given the different regions of influence, our results show that UA and FSI effects remain rather independent for the wind turbine under study, although the spectral analysis of the deformation velocity reveals that the increased unsteadiness introduced by the UA fluctuations starts to trigger the high-frequency structural modes, which also affect the torsional dynamics, with potential effects in the aeroelastic response of the blade when torsion is considered.

The analysis of the fatigue properties from the root reaction components also indicated that the two models have competing effects, whose net balance depends on the reaction component considered. While the FSI-induced aerodynamic damping reduces the load fluctuations almost exclusively at the tip, the hysteresis of the airloads from the UA module increases them more, but primarily at the root, as previously shown for tidal turbines.[92] The DELs confirm the importance of the corrections introduced by the UA model considered and show that classic ALM would underestimate the equivalent loads relevantly, provided that the UA model used is able to produce reliable results.

Finally, the flow dynamics primarily changes because of the different inflow, with increased wave recovery promoted by the more realistic turbulent conditions, but is almost insensitive to the variations induced by the structural vibrations and the UA. Therefore, if one is only interested in the study of the fluid field of similar wind turbines, classic ALM formulation confirms its effectiveness. In addition, the analysis of the mean flow close to the rotor showed the complexity induced by the critical presence of the tower, which affects the definition of the AoA for the blades' airfoils and the airloads in turn.

We acknowledge that the pitching moment UA model needs further studies, given its intrinsic empiricism. But does its use invalidate all the results, especially about the aeroelastic interaction? Since some high-frequency contributions around the torsional natural frequencies are present in the spectra of the flapwise deformation velocity, some effects of the enhanced torsional dynamics start to be observed. However, the flexo-torsional coupling in the blade we considered has a limited importance for the low natural frequencies of the structure, which still remain the dominant ones. Hence, we believe that our conclusions about the FSI coupling are still valid.

In any case, despite the expected limits of the semi-empirical UA model implemented, our study puts under the spotlight the potential impact of the UA on the general dynamic behaviour of the wind turbine and points out the need to further investigate the modelling local aerodynamics for simplified CFD methods used in wind energy. Moreover, severe fluctuations of the AoA may cause higher-frequency and higher-amplitude fluctuations of the aerodynamic coefficients, triggering even more high-frequency structural modes. These include torsional and more coupled structural modes, which thus paves the way for torsion to come into play in the definition of the AoA. As a result, it will be interesting to examine in further developments, how the inclusion of the torsional degree of freedom in the structural feedback[42] changes the aeroelastic response with complete aerodynamics, properly modelled by improved UA models. Moreover, UA phenomena are exacerbated in very long blades,[11] whose nonlinearities could require to improve the overall structural model, by means of nonlinear beam models[93] (better suited to aeroelastically tailored curved blades[94]) and also by including the effect of the tower, of the nacelle, and of the mutual interaction between the blades in the structural dynamics of the full machine.[95]

ACKNOWLEDGEMENT

We acknowledge the Texas Advanced Computing Center (TACC) for having provided us with the computational resources required by this work.

CONFLICT OF INTEREST

The authors declare no potential conflict of interests.

AUTHOR CONTRIBUTIONS

Giacomo Della Posta: Conceptualisation, methodology, software, validation, formal analysis, investigation, data curation, writing - original draft and visualisation. **Stefano Leonardi**: resources, writing - review & editing, funding acquisition and supervision. **Matteo Bernardini**: resources, writing - review & editing, funding acquisition and supervision.

PEER REVIEW

The peer review history for this article is available at https://publons.com/publon/10.1002/we.2789.

DATA AVAILABILITY STATEMENT

The full data set of the LES simulations is on the order of thousands of gigabytes. By contacting the authors, a smaller subset can be made available.

ORCID

Giacomo Della Posta https://orcid.org/0000-0001-5516-9338
Stefano Leonardi https://orcid.org/0000-0002-4570-2255
Matteo Bernardini https://orcid.org/0000-0001-5975-3734

REFERENCES

1. van Kuik GAM, Peinke J, Nijssen R, et al. Long-term research challenges in wind energy – a research agenda by the european academy of wind energy. *Wind Energy Sci*. 2016;1(1):1-39. doi:10.5194/wes-1-1-2016
2. Mendoza V, Bachant P, Wosnik M, Goude A. Validation of an actuator line model coupled to a dynamic stall model for pitching motions characteristic to vertical axis turbines. *J Phys Conf Ser*. 2016;753:22043. doi:10.1088/1742-6596/753/2/022043
3. Mendoza V, Bachant P, Ferreira C, Goude A. Near-wake flow simulation of a vertical axis turbine using an actuator line model. *Wind Energy*. 2019;22(2):171-188. doi:10.1002/we.2277
4. Quarton DC. The evolution of wind turbine design analysis-a twenty year progress review. *Wind Energy*. 1998;1(S1):5-24. doi:10.1002/(SICI)1099-1824(199804)1:1+3.0.CO;2-I
5. Haans W, Mikkelsen R. Airfoil models in the actuator line code assessed with near-wake measurements on a yawed rotor. In: 45th AIAA Aerospace Sciences Meeting and Exhibit; 2012:424.
6. Rasmussen F, Hansen MH, Thomsen K, et al. Present status of aeroelasticity of wind turbines. *Wind Energy*. 2003;6(3):213-228. doi:10.1002/we.98
7. Øye S. Dynamic stall simulated as time lag of separation. In: Proc 4th IEA Symp. Aerodyn. Wind Turb Rome, Italy; 1991:28.
8. Rasmussen F, Petersen J, Winkelaar D, Rawlinson-Smith R. Response of stall regulated wind turbines. stall induced vibrations. RISO-R-691(EN), Roskilde (Denmark), Risoe National Lab., Test Station for Wind Turbines; 1993:1-343.
9. Leishman JG. Challenges in modelling the unsteady aerodynamics of wind turbines. *Wind Energy*. 2002;5(2-3):85-132. doi:10.1002/we.62
10. Leishman GJ. *Principles of helicopter aerodynamics*: Cambridge University Press; 2006.
11. Vijayakumar G, Yellapantula S, Branlard E, Ananthan S. Enhancement of unsteady and 3D aerodynamics models using machine learning. In: J Phys Conf Ser IOP Publishing; 2020:12065.
12. Farsadi T, Kayran A. Classical flutter analysis of composite wind turbine blades including compressibility. *Wind Energy*. 2020;24(1):69-91. doi:10.1002/we.2559
13. Yan C, Archer CL. Assessing compressibility effects on the performance of large horizontal-axis wind turbines. *Appl Energy*. 2018;212:33-45. doi:10.1016/j.apenergy.2017.12.020
14. Sprague MA, Ananthan S, Vijayakumar G, Robinson M. ExaWind: A multifidelity modeling and simulation environment for wind energy. *J Phys: Conf Ser*. 2020;1452(1):12071. doi:10.1088/1742-6596/1452/1/012071
15. Grinderslev C, González Horcas S, Sørensen NN. Fluid–structure interaction simulations of a wind turbine rotor in complex flows, validated through field experiments. *Wind Energy*. 2021;24(12):1426-1442. doi:10.1002/we.2639
16. Spalart PR. Comments on the feasibility of les for wings, and on a hybrid rans/les approach. In: Proceedings of first AFOSR international conference on DNS/LES Greyden Press; 1997:137-148.
17. Mo J-O, Choudhry A, Arjomandi M, Lee Y-H. Large eddy simulation of the wind turbine wake characteristics in the numerical wind tunnel model. *J Wind Eng Ind Aerodyn*. 2013;112:11-24. doi:10.1016/j.jweia.2012.09.002
18. Mikkelsen R, et al. Actuator disc methods applied to wind turbines. *Ph.D. Thesis*: DTU, Kgs. Lyngby, Denmark; 2003.
19. Xie S, Archer C. Self-similarity and turbulence characteristics of wind turbine wakes via large-eddy simulation. *Wind Energy*. 2015;18(10):1815-1838. doi:10.1002/we.1792
20. Lorber P, Covino A, Carta F. Dynamic stall experiments on a swept 3D wing in compressible flow. In: 22nd Fluid Dynamics, Plasma Dynamics and Lasers Conference. AIAA; 1991:1795.
21. Snel H. Scaling laws for the boundary layer flow on rotating wind turbine blades. In: 4th IEA Symp Aerodyn Wind Turbines Rome, Italy; 1991:1-16.
22. St Hilaire AO, Carta FO. Analysis of unswept and swept wing chordwise pressure data from an oscillating naca 0012 airfoil experiment. ADA126797, United Technologies Research Center; 1983.
23. Damiani R, Hayman G, Wang Q, Jonkman JM. Development and validation of a new unsteady airfoil aerodynamics model within aerodyn. In: 34th Wind Energy Symp; 2016:1007.
24. Theodorsen T, Mutchler WH. General theory of aerodynamic instability and the mechanism of flutter. No. NACA-TR-496, NACA; 1935.
25. Wagner H. Über die entstehung des dynamischen auftriebes von tragflügeln. *ZAMM - J Appl Math Mech*. 1925;5(1):17-35. doi:10.1002/zamm.19250050103
26. Küssner HG. *The present stage of development of the problem of wing flutter*: ARC; 1935.
27. von Karman TH, Sears WR. Airfoil theory for non-uniform motion. *J Aeronaut Sci*. 1938;5(10):379-390. doi:10.2514/8.674
28. Lomax H, Heaslet MA, Fuller FB, Sluder L. Two-and three-dimensional unsteady lift problems in high-speed flight. 19930092122, NASA; 1952.
29. Loewy RG. A two-dimensional approximation to the unsteady aerodynamics of rotary wings. *J Aeronaut Sci*. 1957;24(2):81-92. doi:10.2514/8.3777
30. Leishman JG. Validation of approximate indicial aerodynamic functions for two-dimensional subsonic flow. *J Aircr*. 1988;25(10):914-922. doi:10.2514/3.45680
31. Brunton SL, Rowley CW, Williams DR. Reduced-order unsteady aerodynamic models at low reynolds numbers. *J Fluid Mech*. 2013;724:203-233. doi:10.1017/jfm.2013.163
32. Thwaites B. *Incompressible aerodynamics*: Oxford University Press; 1960.
33. Gurevich MI. *The theory of jets in an ideal fluid*: Pergamon Press; 1966.
34. Corke TC, Thomas FO. Dynamic stall in pitching airfoils: Aerodynamic damping and compressibility effects. *Annu Rev Fluid Mech*. 2015;47(1):479-505. doi:10.1146/annurev-fluid-010814-013632
35. Tran CT, Petot D. Semi-empirical model for the dynamic stall of airfoils in view of the application to the calculation of responses of a helicopter blade in forward flight. *Vertica*. 1981;5:35-53.
36. Hansen MH, Gaunaa M, Madsen HA. A beddoes-leishman type dynamic stall model in state-space and indicial formulations. Risø-R-1354(EN), Risø National Laboratory; 2004.
37. Larsen JW, Nielsen SRK, Krenk S. Dynamic stall model for wind turbine airfoils. *J Fluids Struct*. 2007;23(7):959-982. doi:10.1016/j.jfluidstructs.2007.02.005
38. Leishman JG, Beddoes TS. A semi-empirical model for dynamic stall. *J Am Helicopter Soc*. 1989;34(3):3-17. doi:10.4050/JAHS.34.3.3
39. Bachant P, Goude A, Wosnik M. Actuator line modeling of vertical-axis turbines. arXiv preprint arXiv:160501449; 2018.

40. Spyropoulos N, Papadakis G, Prospathopoulos JM, Riziotis VA. Investigating the level of fidelity of an actuator line model in predicting loads and deflections of rotating blades under uniform free-stream flow. *Appl Sci*. 2021;11(24):12097. https://www.mdpi.com/2076-3417/11/24/12097
41. Moriarty PJ, Hansen AC. Aerodyn theory manual. No. NREL/TP-500-36881, NREL, Golden, CO (US); 2005. doi:10.2172/15014831
42. Della Posta G, Leonardi S, Bernardini M. A two-way coupling method for the study of aeroelastic effects in large wind turbines. *Renew Energy*. 2022; 190:971-992. doi:10.1016/j.renene.2022.03.158
43. Santoni C, García-Cartagena EJ, Ciri U, Zhan L, Valerio Iungo G, Leonardi S. One-way mesoscale-microscale coupling for simulating a wind farm in north texas: Assessment against scada and lidar data. *Wind Energy*. 2020;23(3):691-710. doi:10.1002/we.2452
44. Smagorinsky J. General circulation experiments with the primitive equations: I. The basic experiment. *Mon Weather Rev*. 1963;91(3):99-164. doi:10.1175/1520-0493(1963)0912.3.CO;2
45. Sørensen JN, Shen WZ. Numerical modeling of wind turbine wakes. *J Fluids Eng*. 2002;124(2):393-399. doi:10.1115/1.1471361
46. Santoni C, Carrasquillo K, Arenas-Navarro I, Leonardi S. Effect of tower and nacelle on the flow past a wind turbine. *Wind Energy*. 2017;20(12):1927-1939. doi:10.1002/we.2130
47. Troldborg N, Sørensen JN, Mikkelsen RF. Actuator line modeling of wind turbine wakes. *Ph.D. Thesis*: DTU; 2009.
48. Martínez-Tossas LA, Churchfield MJ, Leonardi S. Large eddy simulations of the flow past wind turbines: Actuator line and disk modeling. *Wind Energy*. 2015;18(6):1047-1060. doi:10.1002/we.1747
49. Hansen MH. Improved modal dynamics of wind turbines to avoid stall-induced vibrations. *Wind Energy*. 2003;6(2):179-195. doi:10.1002/we.79
50. Hsu M-C, Bazilevs Y. Fluid–structure interaction modeling of wind turbines: simulating the full machine. *Comput Mech*. 2012;50(6):821-833. doi:10.1007/s00466-012-0772-0
51. Dose B, Rahimi H, Herráez I, Stoevesandt B, Peinke J. Fluid-structure coupled computations of the NREL 5 MW wind turbine by means of CFD. *Renew Energy*. 2018;129:591-605. doi:10.1016/j.renene.2018.05.064
52. Jonkman J, Butterfield S, Musial W, Scott G. Definition of a 5-MW reference wind turbine for offshore system development. NREL/TP-500-38060, Golden, CO (USA), NREL; 2009. doi:10.2172/947422
53. Reschke C. Flight loads analysis with inertially coupled equations of motion. In: AIAA Atmospheric Flight Mechanics Conference and Exhibit; 2005: 6026.
54. Saltari F, Riso C, De Matteis G, Mastroddi F. Finite-element-based modeling for flight dynamics and aeroelasticity of flexible aircraft. *J Aircr*. 2017; 54(6):2350-2366. doi:10.2514/1.C034159
55. Przemieniecki JS. *Theory of matrix structural analysis*: Courier Corporation; 1985.
56. Chung J, Hulbert GM. A time integration algorithm for structural dynamics with improved numerical dissipation: The generalized-α method. *J Appl Mech*. 1993;60(2):371-375. doi:10.1115/1.2900803
57. Felippa CA, Park KC, Farhat C. Partitioned analysis of coupled mechanical systems. *Comput Methods Appl Mech Eng*. 2001;190(24):3247-3270. Advances in Computational Methods for Fluid-Structure Interaction. doi:10.1016/S0045-7825(00)00391-1
58. Heinz JC. Partitioned fluid–structure interaction for full rotor computations using CFD. *Ph.D. Thesis*: DTU, Kgs. Lyngby, Denmark; 2013.
59. Farhat C, Lesoinne M. On the accuracy, stability, and performance of the solution of three-dimensional nonlinear transient aeroelastic problems by partitioned procedures. In: 37th Structure, Structural Dynamics and Materials Conference; 1996:1388.
60. Piperno S. Explicit/implicit fluid/structure staggered procedures with a structural predictor and fluid subcycling for 2d inviscid aeroelastic simulations. *Int J Numer Methods Fluids*. 1997;25(10):1207-1226. doi:10.1002/(SICI)1097-0363(19971130)25:10%3C1207::AID-FLD616%3E3.0.CO;2-R
61. Piperno S, Farhat C. Partitioned procedures for the transient solution of coupled aeroelastic problems–part II: Energy transfer analysis and three-dimensional applications. *Comput Methods Appl Mech Engrg*. 2001;190(24):3147-3170. Advances in Computational Methods for Fluid-Structure Interaction. https://www.sciencedirect.com/science/article/pii/S0045782500003868
62. Farhat C, Lesoinne M. Two efficient staggered algorithms for the serial and parallel solution of three-dimensional nonlinear transient aeroelastic problems. *Comput Methods Appl Mech Engrg*. 2000;182(3):499-515. https://www.sciencedirect.com/science/article/pii/S0045782599002066
63. Storey RC, Norris SE, Stol KA, Cater JE. Large eddy simulation of dynamically controlled wind turbines in an offshore environment. *Wind Energy*; 16(6): 845-864. doi:10.1002/we.1525
64. Meng H, Lien F-S, Li L. Elastic actuator line modelling for wake-induced fatigue analysis of horizontal axis wind turbine blade. *Renew Energy*. 2018; 116:423-437. https://www.sciencedirect.com/science/article/pii/S0960148117308364
65. Trigaux F, Chatelain P, Winckelmans G. A flexible actuator curve model for aeroelastic simulations of wind turbines in atmospheric boundary layers. *J Phys: Conf Ser*. 2022;2265(2):22050. doi:10.1088/1742-6596/2265/2/022050
66. Bazilevs Y, Takizawa K, Tezduyar TE. *Computational fluid–structure interaction: methods and applications*: John Wiley & Sons; 2013.
67. Damiani RR, Hayman G. The unsteady aerodynamics module for fast8. tech. rep., NREL, Golden, CO (US); 2019. doi:10.2172/1576488
68. Sheng W, Galbraith RA, Coton FN. A modified dynamic stall model for low mach numbers. *J Sol Energy Eng*. 2008;130(3):1-10. doi:10.1115/1.2931509
69. Bisplinghoff RL, Ashley H. *Principles of aeroelasticity*: Courier Corporation; 2013.
70. van der Wall BG, Leishman JG. On the influence of time-varying flow velocity on unsteady aerodynamics. *J Am Helicopter Soc*. 1994;39(4):25-36. doi:10.4050/JAHS.39.25
71. Johansen J. Unsteady airfoil flows with application to aeroelastic stability. Risø-R-1116(EN), Risø National Lab; 1999.
72. Liu X, Liang S, Li G, Godbole A, Lu C. An improved dynamic stall model and its effect on wind turbine fatigue load prediction. *Renew Energy*. 2020;156: 117-130. doi:10.1016/j.renene.2020.04.040
73. Leishman JG. Final report: assessment of 'aerodyn' theory basis including unsteady aerodynamics modules. DE-AC36-08GO28308, NREL, Golden, CO (US); 2011.
74. Leishman JG, Beoddoes TS. A general model for airload unsteady behavior and dynamic stall using the indicial method. In: Proc 42nd Annual Forum Am Helicopter Soc. American Helicopter Society; 1986:243-266.
75. Pierce KG. Wind turbine load prediction using the beddoes-leishman model for unsteady aerodynamics and dynamic stall. *Master's Thesis*: University of Utah; 1996.
76. Van Driest ER. On turbulent flow near a wall. *J Aeronaut Sci*. 1956;23(11):1007-1011. doi:10.2514/8.3713

77. Breton S-P, Sumner J, Sørensen JN, Hansen KS, Sarmast S, Ivanell S. A survey of modelling methods for high-fidelity wind farm simulations using large eddy simulation. *Philos Trans Royal Soc A*. 2017;375(2091):20160097. doi:10.1098/rsta.2016.0097
78. Cheng W-C, Porté-Agel F. Adjustment of turbulent boundary-layer flow to idealized urban surfaces: A large-eddy simulation study. *Bound-Layer Meteorol*. 2015;155(2):249-270. doi:10.1007/s10546-015-0004-1
79. Mann J. Wind field simulation. *Probabilistic Eng Mech*. 1998;13(4):269-282. https://www.sciencedirect.com/science/article/pii/S0266892097000362
80. WAsP Engineering. Wind conditions for fatigue loads, extreme loads and siting; 2022. Accessed: August 20, 2022. https://www.wasp.dk/weng#details__iec-turbulence-simulator
81. NREL. Nrel 5 mw baseline airfoils; 2016. [Online; Accessed October 15, 2021]. https://github.com/old-NWTC/FAST/tree/master/CertTest/5MW_Baseline/Airfoils
82. Du Z, Selig M. A 3-d stall-delay model for horizontal axis wind turbine performance prediction. In: 1998 ASME Wind Energy Symp; 1998:21.
83. Eggers A, Chaney K, Holley W, Ashley H, Green H, Sencenbaugh J. Modeling of yawing and furling behavior of small wind turbines. In: 2000 ASME Wind Energy Symp; 2000:20.
84. Phillips CL, Parr JM, Riskin EA. *Signals, systems, and transforms*: Prentice Hall Upper Saddle River; 2003.
85. Ehrich S, Schwarz CM, Rahimi H, Stoevesandt B, Peinke J. Comparison of the blade element momentum theory with computational fluid dynamics for wind turbine simulations in turbulent inflow. *Appl Sci*. 2018;8(12). https://www.mdpi.com/2076-3417/8/12/2513
86. Larsen TJ, Hansen AM. How 2 HAWC2, the user's manual. Risø-R-1597, Roskilde and Kgs. Lyngby, Denmark, Risø National Laboratory, Technical University of Denmark; 2007. https://www.hawc2.dk
87. Sutherland HJ. On the fatigue analysis of wind turbines. tech. rep., Albuquerque, NM (US), Sandia National Labs; 1999. doi:10.2172/9460
88. Buhl ML. MCrunch user's guide for version 1.00. NREL/TP-500-43139, Golden, CO (USA), NREL; 2008.
89. Li N, Liu Y, Li L, et al. Numerical simulation of wind turbine wake based on extended k-epsilon turbulence model coupling with actuator disc considering nacelle and tower. *IET Renew Power Gener*. 2020;14(18):3834-3842. https://ietresearch.onlinelibrary.wiley.com/doi/abs/10.1049/iet-rpg.2020.0416
90. Aitken ML, Banta RM, Pichugina YL, Lundquist JK. Quantifying wind turbine wake characteristics from scanning remote sensor data. *J Atmos Ocean Technol*. 2014;31(4):765-787. https://journals.ametsoc.org/view/journals/atot/31/4/jtech-d-13-00104_1.xml
91. Hansen MOL, Sørensen JN, Voutsinas S, Sørensen N, Madsen HA. State of the art in wind turbine aerodynamics and aeroelasticity. *Prog Aerosp Sci*. 2006;42(4):285-330. doi:10.1016/j.paerosci.2006.10.002
92. Scarlett GT, Sellar B, van den Bremer T, Viola IM. Unsteady hydrodynamics of a full-scale tidal turbine operating in large wave conditions. *Renew Energy*. 2019;143:199-213. doi:10.1016/j.renene.2019.04.123
93. Hodges DH. *Nonlinear composite beam theory*: AIAA; 2006.
94. Wang Q, Sprague MA, Jonkman J, Johnson N, Jonkman B. Beamdyn: A high-fidelity wind turbine blade solver in the fast modular framework. *Wind Energy*. 2017;20(8):1439-1462. doi:10.1002/we.2101
95. Hansen MH. Aeroelastic instability problems for wind turbines. *Wind Energy*. 2007;10(6):551-577. doi:10.1002/we.242
96. Shen WZ, Mikkelsen R, Sørensen JN, Bak C. Tip loss corrections for wind turbine computations. *Wind Energy*. 2005;8(4):457-475. doi:10.1002/we.153
97. Johnson KE, Pao LY, Balas MJ, Fingersh LJ. Control of variable-speed wind turbines: Standard and adaptive techniques for maximizing energy capture. *IEEE Control Syst*. 2006;26(3):70-81. doi:10.1109/MCS.2006.1636311

SUPPORTING INFORMATION

Additional supporting information can be found online in the Supporting Information section at the end of this article.

How to cite this article: Della Posta G, Leonardi S, Bernardini M. Large eddy simulations of a utility-scale horizontal axis wind turbine including unsteady aerodynamics and fluid-structure interaction modelling. *Wind Energy*. 2022;1-28. doi:10.1002/we.2789

APPENDIX A: ROTOR MODELLING

The rotor inside the fluid domain is modelled by the ALM:[45] the airloads are determined by means of a blade-element approach and are then distributed as body forces along rotating lines, which substitute the physical blades in the fluid domain in correspondence of the azimuthal position of the actual blades. According to the blade element theory, for a 2D airfoil the lift force F_l, the drag force F_d and the aerodynamic pitching moment M (referred to the airfoil quarter of chord) per unit length are as follows:

$$F_l = \frac{1}{2}\rho U_{rel}^2 c C_l(\alpha) F, F_d = \frac{1}{2}\rho U_{rel}^2 c C_d(\alpha) F, M = -\frac{1}{2}\rho U_{rel}^2 c^2 C_m(\alpha) F, \tag{A1}$$

where ρ is the air density, U_{rel} is the magnitude of the local relative velocity in the plane of the airfoil, $C_l(\alpha)$, $C_d(\alpha)$ and $C_m(\alpha)$ are the lift, drag and pitching moment coefficients for the local AoA α and F is a modified Prandtl correction factor. The minus sign in M considers the usual convention according to which C_m is positive when it pitches the airfoil in the nose-up direction, which is here the $-E_1$ direction (Figure 3).

To correct the typical overprediction of the airloads at the blade tip and root, due to the finiteness of the blade span, Equation (A1) uses a modified Prandtl tip correction factor,[96] that for the wind turbine considered is given by the following:

$$F=\frac{4}{\pi^2}\cos^{-1}\left[\exp\left(-g\frac{3}{2}\frac{R-r}{r\sin(\alpha+\phi)}\right)\right]\cos^{-1}\left[\exp\left(-g\frac{3}{2}\frac{r-R_h}{r\sin(\alpha+\phi)}\right)\right], \quad \text{with } g=\exp[-0.125(3\lambda-21.0)]+0.1, \tag{A2}$$

where r is the distance from the hub centre, R is the rotor radius, R_h is the hub radius, ϕ is the local pre-twist angle of the blade, $\lambda=\Omega R/U$ is the tip speed ratio and Ω is the rotor angular speed.

Finally, a 2D Gaussian kernel η spreads the local lift and drag in cylindrical regions surrounding each actuator line, to avoid numerical instabilities due to concentrated forces. The actuator lines start from the hub radius and do not extend up to hub centre. Thus, the body force vector $\boldsymbol{f}^t$ in Equation (3) is as follows:

$$\boldsymbol{f}^t=-\boldsymbol{f}^{aero}\eta=-\boldsymbol{f}^{aero}\frac{1}{\epsilon^2\pi}\exp\left[-\left(\frac{r_\eta}{\epsilon}\right)^2\right], \tag{A3}$$

where r_η is the radial distance of a point of the cylinder from the relative actuator line and ϵ is the spreading parameter.

Even though this severe limitation hinders the potential of LES-ALM simulations, the very fine temporal resolution given by the time step limitations bolsters the accuracy and the stability of the FSI coupling methodology. Indeed, the FSI algorithm is at least first-order accurate, even if the interfield parallelism is obtained at the expense of possible amplified errors in the mutual interaction and response of the single fields, as Farhat and Lesoinne[59] report. However, without subcycling the fluid computations, that is, using the same time *sub*step for the solid and the fluid dynamics, it has been demonstrated that a light amplification of the errors appears only in the case of strong instabilities and that adopting a reduced time step, the error produced is even smaller than those corresponding to more sophisticated parallel staggered algorithms.

Finally, an IBM procedure validated in Santoni et al[46] is used for the tower and the nacelle, while the balance between the aerodynamic torque T_{aero} and the generator torque T_{gen} determines the low-shaft angular speed Ω, such that:

$$I_d\dot{\Omega}=I_d\ddot{\Theta}=T_{aero}-T_{gen}=T_{aero}-k_{gen}\Omega^2, \tag{A4}$$

where I_d is the drivetrain rotational inertia, $(\dot{\bullet})$ and $(\ddot{\bullet})$ indicate the first and second time derivatives and Θ is the counterclockwise azimuthal angle indicating the position of a reference blade (Figure 3). A standard quadratic control law[97] characterises the generator torque, where the torque gain k_{gen} is related to the turbine's optimal tip speed ratio ($\lambda_{opt}\approx 7.5$ for the case under study).[52]